Reprint Dec 96

NASA Technical Memorandum 106793

Thermochemical Degradation Mechanisms for the Reinforced Carbon/Carbon Panels on the Space Shuttle

Nathan S. Jacobson
Lewis Research Center
Cleveland, Ohio

and

Robert A. Rapp
The Ohio State University
Columbus, Ohio

January 1995

National Aeronautics and
Space Administration

THERMOCHEMICAL DEGRADATION MECHANISMS FOR THE REINFORCED CARBON/CARBON PANELS ON THE SPACE SHUTTLE

Nathan S. Jacobson
National Aeronautics and Space Administration
Lewis Research Center
Cleveland, Ohio 44135

Robert A. Rapp
Department of Materials Science and Engineering
The Ohio State University
Columbus, Ohio 43210

ABSTRACT

The wing leading edge and nose cone of the Space Shuttle are fabricated from a reinforced carbon/carbon material (RCC). The material attains its oxidation resistance from a diffusion coating of SiC and a glass sealant. During re-entry, the RCC material is subjected to an oxidizing high temperature environment, which leads to degradation via several mechanisms. These mechanisms include oxidation to form a silica scale, reaction of the SiO_2 with the SiC to evolve gaseous products, viscous flow of the glass, and vaporization of the glass. Each of these is discussed in detail.

Following extended service and many missions, the leading-edge wing surfaces have exhibited small pinholes. A chloridation/oxidation mechanism is proposed to arise from the NaCl deposited on the wings from the sea-salt laden air in Florida. This involves a local chloridation reaction of the SiC and subsequent re-oxidation at the external surface. Thermodynamic calculations indicate the feasibility of these reactions at active pits. Kinetic calculations predict pore depths close to those observed.

I. INTRODUCTION

Reinforced carbon/carbon (RCC) material is a remarkably effective thermal protection material, used in the leading edge and nose cone of the space shuttle. This material consists of woven carbon fibers, impregnated with a liquid carbon precursor to fill the voids and then converted to carbon by pyrolysis. Such a material exhibits excellent high temperature mechanical properties, but as is well known, requires virtually perfect oxidation protection.

Oxidation protection is attained via several coating steps (ref. 1). First a diffusion coating of silicon-rich silicon carbide (SiC) is grown at high temperatures using a pack cementation process. Next a coating of tetraethyl orthosilicate (TEOS) is applied via a vacuum impregnation and cured to form silicon dioxide (SiO_2) to plug surface cracks and fissures. The final coating is a Type A sealant, which is a proprietary slurry coating of sodium silicate, SiC, and other compounds. Figure 1 is a micrograph of a polished cross section of this material. The difference in thermal expansion of the carbon substrate and SiC coating leads to cracking of the coating and the fluid glass from the TEOS and Type A sealant is intended to fill these cracks up to the operating temperature.

During a shuttle mission, the RCC material is subjected to high temperature aggressive environments (ref. 2). Before the launch, the shuttle craft is exposed to the salt laden air of Florida for periods of up to a month. More salt is expected to deposit on the wings rather than the nose cone, as the latter is covered by a canopy on the launch pad. These salt deposits are likely to remain on the wings during launch and re-entry, especially if they are trapped in surface cracks and recesses. Launch lasts only for about 8 min and involves temperatures up to 866 K, temperatures far below the melting of boiling points of the salts. Higher temperatures are attained during re-entry, which lasts about 30 min and involves temperatures up to 1977 K. The time to reach temperature is about 5 to 8 min and time at the highest temperature lasts 7 to 8 min. Possible trans-Atlantic (TAL) abort trajectories would involve temperatures to 2095 K.

The re-entry atmosphere is complex, containing a mixture of atoms and molecules of oxygen, nitrogen, and carbon dioxide in a pressure range of about 0.005 to 0.10 atm. These conditions are best simulated with an arc-jet (ref. 1).

During a mission, a number of chemical reactions may lead to material recession and/or localized degradation, such as the pinholes which have been observed on the wing leading edge material after several missions. The purpose of this report is to provide a detailed description of each of the several possible degradation reactions. Specifically, these include:

1. Oxidation. Passive oxidation may convert the SiC to SiO_2(s) and CO(g). Under extreme reducing conditions, especially in very localized spots, the silica and sodium silicate may no longer be stable. Under such a condition of greatly reduced ambient oxygen pressure, solid SiO_2 will not form. Instead, evaporation of the gaseous suboxide, SiO(g), leads to rapid material consumption; this is termed "active oxidation".
2. Reaction of SiO_2 with SiC. This leads to generation of gaseous products and possible bubble formation at the SiC/glass interface.
3. Flow of the sodium silicate.
4. Vaporization of the sodium silicate layer.
5. Sodium chloride (NaCl) induced corrosion. This could involve a reaction of both silica and SiC with chlorine from the NaCl to form volatile $SiCl_x$ (x = 1 to 4) compounds. This process may lead to the observed pinholes, as is analyzed in detail in this report.

II. OXIDATION

Most metals and silicon-based ceramics (e.g., silicon carbide) are not stable in air at high temperatures and form a thin oxide film or scale which acts as a barrier against further attack. There are many reviews of this field (ref. 3 to 5). Examples of protective oxides are NiO on Ni, Al_2O_3 on Ni-Al alloys, and Cr_2O_3 on Ni-Cr alloys. Some materials do not form a solid oxide and hence are unstable in oxygen without a secondary coating. Carbon is, of course, the best example of this, since it oxidizes to form CO(g) and CO_2(g) in a ratio dependent on the temperature and availability of oxygen.

The degree of protection offered by an oxide film depends on its inherent coverage, adherence, and diffusion characteristics. The best protective films have the lowest diffusion coefficient for oxygen; these include alumina (Al_2O_3) and silica (SiO_2). In high temperature oxidizing gases, SiC forms a thin protective film of silica as:

$$SiC(s)\ (2) + 3/2\ O_2(g) = SiO_2(s) + CO(g) \qquad (1)$$

Since oxygen is the mobile species in SiO_2, both SiO_2 and CO form at the SiC/SiO_2 interface. Figure 2 is a schematic illustration of a scale of SiO_2 on SiC, showing the fluxes of O_2 in and CO out, as occurs during the oxidation process. There is general agreement (ref. 5) that the oxidation rate of SiC is limited by the inward diffusion of the O_2, so the growth rate of SiO_2 is inversely proportional to the film thickness. This results in parabolic scale growth as shown in figure 3 for the oxidation of SiC at 1300 °C. Scale growth rates can be measured in either scale thickness or net weight gain of oxygen.

Many factors may influence the diffusivity of oxygen through the silica scale (ref. 5). There is general (but not complete!) agreement in the literature that oxygen diffuses through amorphous silica as a molecule and through crystalline silica as an oxygen anion, and that the diffusivity of oxygen in amorphous silica is greater than in crystalline silica. Amorphous silica tends to form below about 1650 K and tends to crystallize at higher temperatures and/or in the presence of impurities. Grain boundaries in crystalline SiO_2 may provide rapid diffusion paths. The form of oxygen also has an influence on its diffusion rate and corresponding scale growth rate. Atomic oxygen should diffuse through silica faster than molecular oxygen, leading to more rapid scale growth rates.

An important consequence of a diffusion-controlled growth of a thin product scale is a steep gradient in oxygen potential through the scale. For silicon carbide oxidizing in one atmosphere of oxygen, the oxygen pressure at the gas/oxide interface is one atm, and the oxygen partial pressure at the oxide/carbide interface can be as low as 4.3×10^{-23} atm at 1500 K. This is a significant issue in determining the reactivity at this interface.

The protection scheme for the RCC material is unique in that a film of SiO_2 is applied via a vacuum impregnation process to the SiC. At high temperatures, further oxidation of the SiC particles in the Type A sealant and silicon-rich SiC coating on the carbon/carbon is likely to occur via reaction (1). Parabolic oxidation kinetics require that additional silica formation slows the rate as the scale thickens. The oxidation reaction also generates CO(g) as a product, which either dissolves and diffuses through the glass or else forms bubbles. Over very long times and at high temperatures, CO evolution may cause scale rupture and lead to oxidative consumption of the SiC coating.

At very low oxygen pressures, e.g., beneath a stagnant boundary layer of an inert gas, the passive $SiO_2(s)$ becomes unstable and active oxidation may consume the SiC. The transition pressure is derived in Appendix A. Note that active oxidation only occurs for extreme conditions of high temperature and reduced oxygen availability.

In summary, continued thermal oxidation adds silica to the glass coating on the RCC and therefore slows the oxidation rate. Under very low oxygen partial pressures and high temperatures, however, active oxidation and rapid material consumption can occur.

III. REACTION OF SiC AND SiO_2—POSSIBLE BUBBLE FORMATION BENEATH THE SCALE

The silicon carbide/silica system is somewhat unique in that at high temperatures, these components react according to equation (2) to generate volatile products at their mutual interface:

$$SiC + 2\ SiO_2 = 3\ SiO(g) + CO(g) \tag{2}$$

At very high temperatures, this reaction can generate high gas pressures at the SiC/SiO_2 interface (refs. 7 and 8). If the gases do not escape by diffusion, they may form bubbles and disrupt the SiO_2-glass coating. Generally it is assumed that when the total pressure of SiO(g) plus CO(g) exceeds somewhat the ambient pressure, a gas bubble will form. However, the exact conditions for gas bubble formation are much more complex, involving surface tension, nucleation sites, viscous flow, and other factors. The pressures and relative amounts of SiO(g) and CO(g) generated by the above reaction depend on temperature and the thermodynamic activities of Si and C in SiC; in general the 3:1 ratio for SiO to CO gases of equation (2) is not satisfied.

The exact value for the carbon activity in SiC can be calculated from the standard Gibbs energy of formation, $\Delta G°_{SiC}$ and the corresponding equilibrium constant, K:

$$Si + C = SiC \qquad \Delta G° = -61.585\ kJ/mol \text{ at } 1500\ K = -RT \ln K_3 \tag{3}$$

$$K_3 = 139.53 = 1/(a_{Si}a_C) \tag{4}$$

$$\text{For } a_{Si} = 1 \quad a_C = 7.167\times10^{-3}$$

Thus the carbon activity can only vary between 1 (carbon-saturated SiC) and 0.007167 (silicon-saturated SiC) at 1500 K. Correspondingly, the silicon activity can only vary between 0.007167 (carbon-saturated SiC) and 1 (silicon-saturated SiC). If an activity of one component is set, the corresponding activity of the other component is decided. For the reaction of SiC and SiO_2, the pressures of SiO(g) and CO(g) can be calculated for both silicon- and carbon-saturated SiC. The best way to illustrate this is to examine the SiO and CO isobars over the Si-C-O isothermal stability diagram. A recent article by Gaskell (ref. 9) describes the construction of these diagrams in detail.

Stability diagrams with log (a_C) and log (P_{O_2}) as axes are the easiest to construct and probably the most relevant for the RCC case. The diagram shown in figure 4 presents a map of the stable condensed phases for a given carbon activity and oxygen pressure. We are interested in the SiC/SiO_2 interface, which is represented by the line AB in the stability diagram. Any point on this line can be specified by setting an activity of carbon or a partial pressure of oxygen. Point A is carbon-saturated SiC and point B is silicon-saturated SiC.

In practice, identifying a carbon activity and a partial pressure of oxygen by direct measurement is difficult. So we construct isobars of SiO(g) and CO(g) on figure 4. From the isobars, we can approximate the pressures of SiO and CO for carbon-saturated SiC, silicon-saturated SiC, as well as intermediate compositions of SiC. These pressures are given by the intersections of the SiO(g) and CO(g) isobars at the appropriate point on line AB. These values can be calculated for points A and B, respectively, from the following expressions (ref. 7):

Carbon-saturated SiC:

$$\text{For } P_{SiO}\text{:} \quad SiC + SiO_2 = C + 2\ SiO(g) \qquad K_5 = P_{SiO}^2 \tag{5}$$

$$\text{For } P_{CO}\text{:} \quad 3C + SiO_2 = SiC + 2\ CO \qquad K_6 = P_{CO}^2 \tag{6}$$

Silicon-saturated SiC:

$$\text{For } P_{SiO}: \quad Si + SiO_2 = 2\ SiO(g) \qquad K_7 = P_{SiO}^2 \tag{7}$$

$$\text{For } P_{CO}: \quad 2\ SiC + SiO_2 = 3\ Si + 2\ CO \quad K_8 = P_{CO}^2 \tag{8}$$

Table I lists these pressures for a range of temperatures. These results are shown graphically in figure 5, which is a plot of total pressure of CO(g) and SiO(g) for silicon-saturated SiC + SiO_2, carbon-saturated SiC + SiO_2, and SiC + SiO_2, which produces SiO(g) and CO(g) in a 3 to 1 molar ratio according to reaction (2). For figure 5, one atmosphere has been taken as a point of bubble formation. Note that P(SiO) + P(CO) is significantly higher for carbon-saturated SiC than for silicon-saturated SiC. This important difference amounts to about a 250 K temperature advantage for silicon-saturated SiC over carbon-saturated SiC.

Silicon-saturated SiC reacts much less with the SiO_2 glass to generate gaseous products than does carbon-saturated SiC. For this reason the SiC diffusion coating on the carbon/carbon is silicon-rich. This is also the reason why Si particles would be preferred to SiC particles in any slurry sealant intended to plug holes in the SiC coating.

IV. FLOW OF THE GLASS

The Type A sealant is a sodium silicate glass. There is clearly a correspondence of viscosity to temperature and certainly to Na content as well. At temperatures below the maximum re-entry temperature, the glass is molten and tends to flow. This is beneficial in that it will fill any cracks in the SiC that result from the thermal expansion mismatch with the RCC. However, if NaCl is present at the base of these cracks, the flow of glass will not displace this NaCl which may still lead to some damage. This will be discussed in section VI. In addition, if the glass flows too much, it may be blown off the surface by viscous drag, exposing the SiC and possibly the carbon/carbon itself to attack.

V. VAPORIZATION OF THE GLASS

Let us first consider SiO_2 and the gas phase alone. Figure 6 shows a volatility diagram for SiO_2 on Si at 1800 K. We are concerned with the SiO_2 portion of this diagram as it exists on an SiC substrate or coating. Several references describe the construction of these diagrams (ref. 4, 10 and 11). For a given temperature, such a diagram plots the partial pressures of the various vapor species above a condensed phase as a function of oxygen pressure. Note that $SiO_2(s)$ does not only vaporize to $SiO_2(v)$, but rather to several different species. Increasing the oxygen pressure suppresses vaporization of SiO, but has no effect on the vaporization of SiO_2 to $SiO_2(g)$. Qualitatively, this can be seen from the reactions:

$$SiO_2(s) = SiO(g) + 1/2\ O_2(g) \tag{9}$$
$$\text{with } d \log P_{SiO}/d \log P_{O_2} = -1/2$$

$$SiO_2(s) = SiO_2(g) \tag{10}$$
$$\text{with } d \log P_{SiO_2}/d \log P_{O_2} = 0$$

The outer coating on the RCC materials is the Type A sealant, which is primarily a sodium silicate glass. There are several sodium silicate glass compositions with different ratios of Na_2O to SiO_2. Since this glass is in contact with the SiO_2 from TEOS, it likely becomes the most silica-rich composition—$Na_2Si_2O_5$. We can construct a volatility diagram for $Na_2Si_2O_5$. However, this is a more complex system than SiO_2 and can be handled another way.

In the case of a sodium silicate glass, Na is expected to vaporize preferentially. Since this involves a decomposition, oxygen is expected to suppress the volatility of Na. The best way to calculate vapor pressures is with a free energy minimization type computer code (refs. 12 and 13). Such a code considers all the atoms from a given system and determines the products with the minimum free energy. The vapor pressure can be calculated for a vacuum or for a system with a given over-pressure of gas. Figure 7 shows that calculated vapor pressures above $Na_2Si_2O_5$ in vacuum and figure 8 shows the calculated vapor pressures above $Na_2Si_2O_5$ in 0.05 atm oxygen. Note that Na is the primary vapor species and that 0.05 atm oxygen suppresses the vapor pressure of Na by more than two orders of magnitude. These are thermodynamic (equilibrium) vapor pressures.

From the standpoint of kinetics, the maximum possible vapor flux (ref. 14) for a given vapor pressure can be calculated from the Hertz-Langmuir expression:

$$J = \alpha P/(2\pi MRT)^{1/2} \tag{11}$$

where J is a flux in mole/(unit area-unit time), α accounts for stearic and other kinetic limitations and any backflux of species (ref. 14), M is the molecular weight of the gas, R is the gas constant and T is the absolute temperature. The total evaporation rate comprises the sum of fluxes calculated for each vapor species. This maximum possible vapor flux of equation (11) is observed in a vacuum or rapidly flowing gas with no boundary layer. In most problems, a boundary layer is present and the evaporation is limited by gaseous diffusion, as described by the expression:

$$J = h_m(P-P_g) \tag{12}$$

Here P_g is the pressure of the vaporizing species in the carrier or ambient gas (which is often negligible) and h_m is the mass transfer coefficient. Semi-empirical values for h_m are tabulated for a variety of geometries (ref. 15).

The experimental measurement of vapor pressures and evaporation fluxes is a large area of research (ref. 16). The easiest way to measure fluxes is with interrupted or continuous weight loss. Continuous weight loss involves suspending the specimen from a balance in a furnace and continuously monitoring the weight change; a schematic of such a system is shown in figure 9. In these types of measurements, there are two approaches. One involves measuring "Langmuir" evaporation from a free surface into a vacuum. The other involves containing the sample in a Knudsen cell, which is a small enclosure with a well defined orifice for vapor sampling. This enclosure allows the gas and the condensed phase to approach equilibrium, so that a near equilibrium vapor pressure evolves from the cell.

Because weight-change measurements only give total vapor fluxes, some method of analysis is necessary to determine the vapor composition. Perhaps the most valuable method is mass spectrometry (ref. 14). A Knudsen cell is generally used in these systems, since the vapor must be columnated as a molecular beam. Such a mass spectrometer can measure pressures only as high as about 10^{-4} atm. Sampling higher pressures requires a series of differentially pumped vacuum chambers (ref. 15). These mass spectrometric systems can sample condensible gases, such as SiO, Na, and NaO as well as noncondensible gases, such as CO, CO_2, and O_2. A gas chromatograph can also be used at higher pressures, but it can only sample noncondensible gases.

Another method of studying vaporization involves rapid laser heating and using a mass spectrometer to probe the composition of the resultant plume (ref. 18). Such a test may be more relevant to the rapid heating encountered in re-entry.

In summary, the Type A sealant is expected to vaporize preferentially to lose Na. The pressure of oxygen in the re-entry environment will suppress this to some degree. Vapor pressures can be calculated with free energy minimization computer codes and the corresponding maximum possible weight loss rates are calculated from the highest vapor pressures. Vapor fluxes and vapor compositions can be measured experimentally using a gravimetric balance and a mass spectrometer, respectively.

VI. NaCl INDUCED CORROSION

It is well-known that NaCl is an aggresive species in a variety of corrosive environments. In low temperature aqueous environments Cl^- from NaCl is an aggressive anion, promoting pitting (refs. 19 and 20). In high temperature combustion environments, NaCl combines with sulfur impurities in the fuel and water vapor to form the highly stable Na_2SO_4 molecule. Deposits of fused Na_2SO_4 can be highly corrosive (refs. 4 and 5).

In the case of the RCC material on the shuttle, evidence suggests that yet another form of NaCl-induced attack may be occurring. As mentioned, the shuttle can reside on the lauch pad for weeks with the RCC material of the wings exposed to the moist salty seabreezes. Thermal excursions of the RCC material lead to extensive craze cracking of the solidified Type A sealant. A micrograph of this is shown in figure 10. Generally, these surface flaws are not repaired or filled between flights, and therefore they can serve as sites where sea salt is retained and protected from loss by the aerodynamic forces upon ascent. In the analysis which follows, sea salt stored in surface cracks is considered to be heated upon reentry to high temperature where degradative reactions can result. Pinhole formation is suggested to result from a cyclic chloridation/oxidation of silicon carbide, with the formation of a condensed nonprotective silica fume.

VI A. THERMODYNAMICS

As discussed in section V, the computer-assisted analysis of multicomponent, multiphase equilibria between several condensed phases and a gas phase can be performed by a free energy minimization program to calculate the partial pressures of the product vapor species (refs. 12 and 13). To some extent, the results depend upon the phases that are assumed to be present, but the **amounts** of stable condensed phases do not matter, so long as the phases are retained at unit thermodynamic activity. Likewise, the partial pressures of the nitrogen and oxygen gases and the total gas pressure should not be important to this thermodynamic analysis, because volatile nitrogen compounds are not very stable, and the oxygen is already accounted for by assuming that silica is present (or not present). For the calculated results presented in tables II and VII, covering the temperature range from 1200 to 1700 °C (2192 to 3092 °F), the condensed phases SiC and NaCl are assumed to be present, in equilibrium with either carbon or else with silicon, and either in the **presence** of silica (**passive reaction**) or else in the **absence** of silica (**active reaction**). The ambient gas atmosphere is assumed to be pure nitrogen at 1 atm pressure, because some specification of total pressure is required by the program. In fact, for the thermodynamic considerations, the total pressure and the ambient gas composition do not affect the calculated results if the condensed phases are specified.

From the Si-C-O phase stability diagram of figure 11 for 2000 K, the coexistence of SiC and SiO_2 can only lie along a line limited by a further equilibrium with either carbon or else with silicon. Then to examine the full range of values possible, tables II to VII provide the results of calculations for the vapor pressures of species for the 4-phase equilibrium of NaCl + SiC + SiO_2 + C (point A of fig. 12), or else for NaCl + SiC + SiO_2 + Si (point B). In this case, the microenvironment in the pinhole is assumed to be sufficiently oxidizing that SiO_2 exists (passive reaction). Additionally, for the proposed case that the local pinhole environment actually becomes "active" due to the total evaporative loss of SiO_2, the 3-phase equilibria for NaCl + SiC + C (point D) and for NaCl + SiC + Si (point E) have also been evaluated. These four sets of equilibria should bracket any possible set of service conditions for passive oxidation, and for active oxidation, in the NaCl-contaminated pinhole.

Figure 12 summarizes the calculated results for the points A and B of figure 11, as presented in detail in tables II and VII for the condition of passive reaction, i.e., that silica in the pinhole is not totally consumed by the evaporation reactions. For any given temperature, the highest vapor pressures are exhibited by NaCl, which species can boil out of the crack (depending upon the ambient temperature and pressure). The partial pressures for CO, SiO, $SiCl_2$, etc. are plotted as a small range of values for a given temperature, corresponding to the total possible range between equilibrium with carbon or else with silicon. For a qualitative understanding of the degradation mechanism, this **range** for the values is not important. However, as the temperature is raised, the magnitudes of both SiO and $SiCl_2$ vapor are high enough to support a significant flux of silicon from the base of the pit to the surface.

Figure 13 summarizes the detailed results for the points D and E of figure 11, as presented in detail in tables II to VII, for the condition of active (silica-free) reaction in the pinhole. Again the **range** in the possible values is not very important. In form and magnitude, the results for figure 13 are rather similar to those for figure 12. Thus, in the presence of condensed NaCl, except for the absence of the volatile oxides SiO and CO, a large difference is not expected between "passive" and "active" vaporization of SiC in a pinhole.

VI B. CHLORIDATION/OXIDATION REACTION MECHANISM

Figure 14 shows schematically a reaction sequence which rationalizes the generation and growth of pinholes through the SiC coating on carbon/carbon. In figure 14(a), sea salt is condensed into the cracks and crazes of the SiC coating as the shuttle is exposed to the ambient Florida environment. Since the cracking and salt deposition occurs at low temperature, only very little oxide should be present in the crack. During the minor heating upon ascent, in the face of high aerodynamic pressure, the salt would be retained in the crack until reentry, when the high temperature would melt the salt and initiate the reactions indicated in figure 14(b), leading to an evaporative loss of NaCl, SiO, CO and $SiCl_2$. This transient reaction stage corresponds to the "passive" reaction of SiC/SiO_2 described in figure 14(b). Because of the very limited amount of oxygen in the crack, all this oxygen should be lost by SiO and CO formation before the NaCl is lost. Thereafter, as shown schematically in figure 14(c), the base of the pit should suffer "active" chloridation leading to $SiCl_2(v)$ loss.

At the external surface, the $SiCl_2$ vapor would encounter oxygen by collisions with the ambient gas phase. Because in contact with some oxygen, condensed silica is a much more stable phase, the volatile $SiCl_2$ (and any SiO) species would react to form a solid (particulate) fume of SiO_2, as shown schematically in figure 14(c). The relevant reaction at the external surface is:

$$SiCl_2(v) + O_2(g) = SiO_2(fume) + 2\ Cl(g) \quad (13)$$

The atomic chlorine product species are trapped within the pinhole, and diffuse back to the base of the pinhole to repeat the reaction to form $SiCl_2(v)$, as shown schematically also in figure 15(a). There are several possible mechanisms for the removal of carbon from SiC at the base of the pinhole. The carbon could diffuse away into the Si-saturated SiC, or else it might be removed as a volatile species, e.g. some hydrocarbon molecule if any hydrogen is present in the pit. In any case, carbon removal is not thought to be involved in rate control. The fume particles at the surface constitute a porous, non-protective deposit. (Actually, such condensed fume is seen smeared across the external surface of the SiC coating of the shuttle leading edge) The formation of this porous surface deposit is important to the mechanism, because it limits the entry of oxygen from the ambient into the pinhole, an action which would otherwise repassivate the SiC by silica formation in the pinhole.

Such a chloridation/oxidation reaction model has many analogs in systems that have been well studied. The generation of fume resulting from the evaporation of liquid metals was described expertly by Turkdogan, Grieveson and Darken (ref. 21). Hinze and Graham (ref. 22) found copious $Si0_2$ fume as a product of the active oxidation of solid Si. Internal vapor transport cycles are well known in the chloridation of alloys (refs. 23 to 26). If one excludes the electrochemical aspects for materials attack in electrolytic media, this mechanism is quite similar to the localized aqueous corrosion (pitting) of alloys which form passive films in oxygenated environments (refs. 19 and 20). During the pitting of such alloys, chloride and hydrogen ions are concentrated in the pits, where the local environment differs greatly from the bulk solution, and the alloy suffers active corrosion.

VI C. KINETICS OF THE CHLORIDATION/OXIDATION REACTION-RATE OF PINHOLE GROWTH

To analyze the rate at which pinholes should grow/deepen according to the mechanism just proposed, one needs to decide whether the diffusion of reactant and product gas species in the pinhole occurs by Knudsen (free molecular) diffusion (for $l_i >> d$) or else by viscous diffusion (for $l_i << d$), where l_i is the mean free path for species i and d is the characteristic dimension of the system (diameter of the pinhole). The following parameters bracket the conditions in the pinhole:

Temperature range:	1500 to 2100 K
Diameter range of pinholes:	380 to 510 mm (0.015 to 0.020 in.)
Total pressure in pinhole:	0.01 to 0.07 atm

Actually, the pressure in the pinhole has been estimated on the basis of the shock wave against the wing leading edge.

VI C.1. MEAN FREE PATHS

To calculate the mean free path of a species in the gas phase, the diameter of the species is required, but these are not always available. From reference 27, the diameter of N_2 is 3.798 Angstroms. Although there are no data available for the diameter of $SiCl_2(v)$, its diameter can be estimated by a linear interpolation between SiCl(v) and $SiCl_4(v)$. Reference 28 shows that the diameters for CCl_x, BCl_x, and CF_x are linearly dependent upon x. According to this interpolation, the molecular diameter for $SiCl_2(v)$ is 4.491 Angstroms, as listed in table VIII.

The mean free path of a species i at temperature T is given by (ref. 28):

$$l_i = 1/[(2)^{1/2}\pi n_i d_i^2] = k_B T/[(2)^{1/2}\pi P_i d_i^2] \quad (14)$$

where n_i and P_i are the density and partial pressure of i, and k_B the Boltzmann constant. For the model and calculations to follow, the interdiffusion of the vapor species N_2 and $SiCl_2$ are considered to be most important. To consider collisions between N_2 and $SiCl_2$, the summation of the radii for N_2 and $SiCl_2$ is set as d_i and P_{N_2} as P_i in equation (14); the calculated results are listed in table IX.

The mean free paths of $SiCl_2$ should be somewhat smaller than those listed in table IX because of the collisions between $SiCl_2$ molecules. According to the plot of partial pressure profiles of figure 15(b), atomic chlorine has a range of pressure which is nearly twice that for $SiCl_2$, but its atomic diameter is smaller (table VIII), and its diffusional transport should not be rate limiting. The measured diameters of the pinholes are in a range of 380 to 510 mm, which are much

larger than the mean free paths for $SiCl_2$ at temperatures of 1500 to 2100 K. Therefore, **viscous diffusion** of $SiCl_2$ should control the transport of $SiCl_2$ in pinholes and not Knudsen (free molecular) diffusion. A simplification of the microenvironment of the pinhole gas phase to a N_2-$SiCl_2$ binary system can be made for calculation of the diffusivity of $SiCl_2$ in a pinhole.

VI C.2. DIFFUSION CALCULATIONS

The model shown in figure 15(a) was proposed for the growth of a pinhole in SiC. The gradient for $SiCl_2$ pressure in the pinhole supports the diffusion of $SiCl_2$ through the N_2 "background gas" outward to the surface, as shown in figure 15(b). Equation (13) describes the fume-forming reaction at the external surface. Theories for calculating the diffusivity in a binary system are still not well developed, but some empirical equations are available for calculation of the diffusivity. The following equation is used to calculate the diffusivity of $SiCl_2$ in N_2 (ref. 15):

$$D_{SiCl_2\text{-}N_2} = \frac{2}{3}\left(\frac{k_B^3}{\pi^3}\right)^{1/2}\left(\frac{1}{2m_{SiCl_2}} + \frac{1}{2m_{N_2}}\right)^{1/2}\frac{T^{3/2}}{p\left(\frac{d_{SiCl_2} + d_{N_2}}{2}\right)^2} \tag{15}$$

Here $D_{SiCl_2\text{-}N_2}$ is the diffusivity in cm^2/sec, k_B is the Boltzmann constant, m_i is the weight per molecule (i.e., molecular weight/Avogadro Number), T is the absolute temperature, p is the total pressure, and d_i are the molecular diameters. The calculated results are listed in table X. The flux of $SiCl_2(v)$ in the pinhole shown in figure 15 is given by:

$$J_{SiCl_2} = -D_{SiCl_2}\frac{dC_{SiCl_2}}{d\xi} = \frac{D_{SiCl_2}P_{SiCl_2}}{\xi RT} \tag{16}$$

where D_{SiCl_2} is the diffusivity calculated in equation (15), $dC_{SiCl_2}/d\xi$ is the concentration gradient, ξ is the depth of the pinhole, and P_{SiCl_2} is the vapor pressure of $SiCl_2$ in the presence of NaCl and SiC, but in the absence of O_2. The pressure of $SiCl_2$ is from carbon-saturated SiC, since the chloride forming reaction releases carbon (fig. 14(c)). Every mole of $SiCl_2$ formed corresponds to one mole of SiC removed, so $J_{SiCl_2} = J_{SiC}$. The growth (penetration) rate of the pinhole is related to the flux as follows:

$$\frac{d\xi}{dt} = V_{SiC}\,J_{SiC} = V_{SiC}\frac{D_{SiCl_2}P_{SiCl_2}}{\xi RT} \tag{17}$$

where V_{SiC} is the molar volume of SiC (12.43 cm^3/mol). Upon integration of equation (17):

$$\xi^2 = \frac{2\,V_{SiC}\,D_{SiCl_2}\,P_{SiCl_2}}{RT}\,t = k_p t \tag{18}$$

The parabolic rate constants k_p for the pinhole growth are calculated and listed in table XI. The calculated pinhole growth kinetics are plotted in figure 16 for 1200 to 1700 °C at total pressures of 0.01 and 0.07 atm. The extreme condition for the shuttle service can amount to 7.5 to 8 min at a temperature of 1600 °C. These conditions have been highlighted in figure 16, and they correspond to a calculated depth for pinhole penetration of 490 to 1340 μm (19 to 53 mils). Three specific pinholes have been studied in some detail (ref. 29), two pinholes in R/H panel #7 had depths of 15 and 28 mils,

and a pinhole in R/H T-seal R/S 11 had a depth of 15 mils. Considering the uncertainties and approximations, such agreement between analysis and observation may be considered fortunate. On the other hand introduction of a tortuousity factor into equations (17) and (18) to account for the turns in the capillary brings about very good agreement. Indeed, the chloridation/oxidation mechanism represents a logical interpretation for pinhole formation. Clearly, the presence of a fume at the pinhole entrance/exit has been observed at the RCC surface of the shuttle.

In summary, it is possible that the observed pinholes form from the following mechanism. The sea salt deposited on the exposed wing surfaces very likely collects in the cracks in the glass sealant. This can penetrate to the SiC surface and react to form silicon chlorides during re-entry. The silicon chlorides are oxidized to SiO_2 fume at the surface and the chlorine is released to form more silicon chlorides. Thermodynamic calculations indicate the feasiblity of such reactions. Kinetic calculations predict pit depths close to those measured.

VI C.3 STOPPAGE AND AVOIDANCE OF PINHOLES

The chloridation/oxidation mechanism presented here provides answers for a number of problem questions which are tied to pinholes in the SiC coating on the shuttle:

Question 1: Why have pinholes never been observed or simulated in the arc jet or other thermal exposure testing of the materials? Answer: Such test coupons were not provided with imbedded seasalt prior to exposure.

Question 2: Why does the nose cone, which experiences the same thermal service cycle as the leading wing edges, suffer only limited pinhole formation? **Answer:** On the launch pad, the nose cone is covered by a canopy which prevents contact with salt spray.

Question 3: How can one prevent pinhole formation? **Answer:** As soon as possible after the shuttle lands, the wing panels should be sprayed or painted with some sealant to fill in the surface cracks so that salt contamination is not gathered into surface cracks either in transport or in position on the launch pad. A vacuum impregnation is recommended. A canopy should cover the wings of the shuttle on the launch pad until shortly before takeoff.

Question 4: What can be done to clean out existing pinholes and prevent further growth? **Answer:** Perhaps one can clean out the existing pinholes with an element which forms a quite stable volatile chloride, oxide, and oxychloride so that any residual chlorine can be extracted from the pinholes without the formation of a blocking porous oxide fume deposit. The elements Cr and Mo both satisfy this requirment, although Cr is preferred. If the open pinholes were provided with a chromic acidic wash, then upon heating in the presence of oxygen, $CrO_3(v)$ and $CrO_2Cl_2(v)$ should form to clean out the pinhole at temperatures lower than those where $SiCl_2(v)$ reaches a high vapor pressure.

VII. SUMMARY AND CONCLUSIONS

The RCC material is exposed to high temperatures and aggressive environments at several points in a typical mission. Several possible degradation modes have been discussed:

1. Passive oxidation of the SiC coating and SiC particles in the slurry. At extreme conditions of high temperature and low oxygen pressure, the transition to rapid active oxidation may occur.
2. Reaction between SiC and SiO_2. For carbon-saturated SiC this reaction would lead to a high CO(g) pressure generated at the SiC/SiO_2 interface; silicon-saturated SiC is best for minimizing this pressure.
3. Vaporization of the glass. The sodium component is expected to vaporize preferentially. This would be minimized by an overpressure of oxygen.
4. NaCl induced corrosion. This may act to volatilize the protective glass and lead to local pitting. A chloridation/oxidation mechanism causing active reaction of SiC at the base of the pit leads to the deposition of a porous SiO_2 fume at the mouth of the pit and recycling of the atomic chlorine reactant. Extended or repeated operation of this degradation mechanism can explain the pinholes observed in the shuttle leading wing surfaces.

ACKNOWLEDGEMENT

It is a pleasure to thank Drs. Ge Wang and Xuejin Zheng of The Ohio State University for assistance with the calculations.

REFERENCES

1. S.D. Williams, D.M. Curry, D.C. Chao, and V.T. Pham, "Ablation Analysis of the Shuttle Orbiter Oxidation Protected Reinforced Carbon Carbon," AIAA 94–2084, 6th AIAA/ASME Joint Thermophysics and Heat Transfer Conference, June 20–23, 1994, Colorado Springs, CO.
2. D.M. Curry, private communication.
3. P. Kofstad, High Temperature Corrosion, Elsevier Applied Science, New York, 1988.
4. R.A. Rapp, High Temperature Corrosion, ACS Audio Course, American Chemical Society, 1980.
5. N.S. Jacobson, J. Am. Ceram. Soc. 76 [1], 3 (1990).
6. M.A. Lamkin, F.L. Riley, and R.J. Fordham, J. Eur. Ceram. Soc. 10, 347 (1992).
7. R.A. Rapp and G.R. St. Pierre, "New Options for the Protection of Carbon/Carbon Composites," AFWAL-TR–87–4142, R.J. Kearns and L.S. Theibert, eds., p. 27.
8. N.S. Jacobson, K.N. Lee, and D.S. Fox, J. Am. Ceram. Soc. 75 [6] 1603 (1992).
9. D.R. Gaskell, "Phase Equilibria in Si-C-O Ceramic Matrix Composites," CIAC Newsletter, US Department of Defense Information Analysis Center, Purdue University, Vol. 1, No. 3, June 1991.
10. F.J. Kohl, D.M. Leisz, G.C. Fryburg, and C.A. Stearns, "Thermochemical Analyses of the Oxidative Vaporization of Metals and Oxides by Oxygen Molecules and Atoms," NASA Rept. No. TM X–73682, NASA Lewis Research Center, Cleveland, OH, 1977.
11. A.H. Heuer and V.L.K. Lou, J. Am. Ceram. Soc. 73 [10], 2789 (1990).
12. T.M. Besmann, "SOLGASMIX-PV: A Computer Program to Calculate Equilibrium Relationships in Complex Chemical Systems," Rept. No. ORNL/TM-5775, Oak Ridge National Laboratory, Oak Ridge, TN, 1977.
13. W.T. Thompson, A.D. Pelton, and C.W. Bale, Facility for the Analysis of Chemical Thermodynamics (F*A*C*T), University of Montreal, Montreal, Canada.
14. A.W. Searcy, "The Kinetics of Evaporation and Condensation Reactions," in Chemical and Mechanical Behavior of Inorganic Materials, ed. by A. W. Searcy, D.V. Ragone, and U. Columbo, Wiley-Interscience, New York, 1968.
15. G.H. Geiger and D.R. Poirier, Transport Phenomena in Metallurgy, Addison-Wesley, 1974.
16. J.L. Margrave, ed., The Characterization of High Temperature Vapors, Wiley, New York, 1967.
17. C.A. Stearns, F.J. Kohl, G.C. Fryburg, and R.A. Miller, "A High Pressure Modulated Molecular Beam Mass Spectrometric Sampling System", NASA TM–73720, NASA Lewis Research Center, Cleveland, OH, 1977.
18. P.K. Schenk, D.W. Bonnell, and J.W. Hastie, "In Situ Analysis of Laser-Induced Vapor Plumes," in Materials Chemistry at High Temperatures, Volume 2: Processing and Performance, ed. by J.W. Hastie, Humana Press, New Jersey, 1990.
19. H. Kaesche, Metallic Corrosion, translated by R.A. Rapp, NACE, Houston, TX, 1985, pp. 321-324.
20. M.G. Fontana, Corrosion Engineering, McGraw-Hill Publ., NY, (1986), p. 67.
21. E.T. Turkdogan, P. Grieveson, and L.S. Darken, J. Phys. Chem., **67** (1963) 1647.
22. J.W. Hinze and H.C. Graham, J. Electrochem. Soc., **123** (1976) 1066.
23. Y.S. Kim and H.W. Pickering, Metall. Trans. **13B** (1982) 349.
24. L.S. Singheiser, W. Auer, and H. Kaesche, Ber. Bunsenges. Phys. Chem. **87** (1983) 112.
25. R.A. Rapp, J. Physique IV, Colloque C9, suppl. J. Physique III, **3**, (1993) 1.
26. M.J. McNallan, W.W. Lee, S.H. Kim, and C.T. Kang, "Acceleration of the High Temperature Oxidation of Metals by Chlorine," in High Temperature Corrosion, ed. by R.A. Rapp, NACE, Houston, TX, 1981.
27. R.A. Svehla, "Estimated Viscosities and Thermal Conductivities of Gases at High Temperatures", NASA TR–132.
28. C. Kittel and H. Kroemer, Thermal Physics, 2nd Edition, W.H. Freeman, San Francisco, CA, 1980, pp. 389–422.
29. Presentation at NASA JSC, August 2, 1993.
30. S.V. Christensen, "Effect of Mission Induced Pin Holes on RCC Design Life."

TABLE I.—PARTIAL PRESSURE (atm) RANGE FOR SiO AND CO AT THE SiC/VITREOUS SiO_2 INTERFACE

Temperature K (°F)	P_{SiO}-carbon saturated	P_{CO}-carbon saturated	P_{SiO}-silicon saturated	P_{CO}-carbon saturated
1200 (1701)	2.23×10^{-8}	6.07×10^{-5}	5.47×10^{-7}	4.10×10^{-9}
1300 (1881)	4.13×10^{-7}	6.08×10^{-4}	7.66×10^{-6}	9.54×10^{-8}
1400 (2061)	5.00×10^{-6}	4.35×10^{-3}	7.28×10^{-5}	1.41×10^{-6}
1500 (2241)	4.30×10^{-5}	2.37×10^{-2}	5.09×10^{-4}	1.43×10^{-5}
1600 (2421)	2.81×10^{-4}	1.04×10^{-1}	2.77×10^{-3}	1.09×10^{-4}
1700 (2601)	1.46×10^{-3}	3.82×10^{-1}	1.20×10^{-2}	6.79×10^{-4}
1800 (2781)	6.24×10^{-3}	1.21	4.05×10^{-2}	4.42×10^{-3}
1900 (2961)	2.28×10^{-2}	3.35	1.19×10^{-1}	2.35×10^{-2}
2000 (3141)	7.29×10^{-2}	8.34	3.14×10^{-1}	1.05×10^{-1}

TABLE II.—CALCULATED ACTIVITIES FOR GASEOUS AND CONDENSED SPECIES WITH DIFFERENT CONDENSED PHASES PRESENT AT 1200 °C (2192 °F)

Species	SiC + NaCl + SiO_2 + Si	SiC + NaCl + SiO_2 + C	SiC + NaCl + Si	SiC + NaCl + C
N_2	0.906752	0.89744	0.90704	0.907346
NaCl	0.057474	0.05747	0.05747	0.0574737
Na_2Cl_2	0.035083	0.03508	0.03508	0.0350828
SiO	0.000275	0.00988	0	0
Na	0.000269	6.60×10^{-5}	0.00027	6.61×10^{-5}
$SiCl_2$	0.00013	3.20×10^{-5}	0.00013	2.84×10^{-5}
CO	1.49×10^{-5}	2.80×10^{-5}	0	0
$SiCl_3$	2.50×10^{-6}	2.20×10^{-6}	2.50×10^{-6}	2.22×10^{-6}
$SiCl_4$	1.65×10^{-7}	5.90×10^{-7}	1.60×10^{-7}	5.94×10^{-7}
Cl	6.54×10^{-8}	2.70×10^{-7}	6.50×10^{-8}	2.66×10^{-7}
SiCl	3.24×10^{-8}	8.40×10^{-8}	3.20×10^{-8}	1.73×10^{-9}
Si	5.17×10^{-9}	1.70×10^{-9}	5.20×10^{-9}	6.80×10^{-11}
Na_2	2.85×10^{-9}	1.70×10^{-10}	2.90×10^{-9}	1.72×10^{-10}
CO_2	1.45×10^{-11}	6.80×10^{-11}	0	0
SiO_2	3.21×10^{-12}	3.10×10^{-11}	0	0
Cl_2	1.84×10^{-12}	3.20×10^{-12}	1.80×10^{-12}	3.05×10^{-11}
NO	8.53×10^{-15}	7.40×10^{-14}	0	0
NaO	2.08×10^{-16}	4.50×10^{-16}	0	0
SiC	4.60×10^{-18}	4.60×10^{-18}	4.60×10^{-18}	4.60×10^{-18}
N_2O	4.97×10^{-19}	4.29×10^{-18}	0	0
O_2	9.79×10^{-24}	7.44×10^{-22}	0	0
NO_2	3.21×10^{-28}	2.43×10^{-26}	0	0
Condensed				
SiC	1	1	1	1
SiO_2	1	1	0	0
Si	1	0.01315	1	0.0131503
NaCl	1	1	1	1
$Na_2Si_2O_5$	0.000197	0.0001	0	0
Na_2SiO_3	2.4×10^{-5}	1.20×10^{-5}	0	0
C	0.01315	1	0.01315	1

TABLE III.—CALCULATED ACTIVITIES FOR GASEOUS AND CONDENSED SPECIES WITH DIFFERENT CONDENSED PHASES PRESENT AT 1300 °C (2372 °F)

Species	SiC + NaCl + SiO_2 + Si	SiC + NaCl + SiO_2 + C	SiC + NaCl + Si	SiC + NaCl + C
N_2	0.777301	0.733075	0.779007	0.780047
NaCl	0.144609	0.144609	0.144609	0.144609
Na_2Cl_2	0.0749444	0.0749444	0.0749444	0.0749444
SiO	0.00157338	0.00022283	0	0
Na	0.00096278	0.00026971	0.00096278	0.00026971
$SiCl_2$	0.00046709	0.00011938	0.00046709	0.00011938
CO	0.0001328	0.0467481	0	0
$SiCl_3$	8.76×10^{-6}	7.99×10^{-6}	8.76×10^{-6}	7.99×10^{-6}
$SiCl_4$	4.31×10^{-7}	1.41×10^{-6}	4.31×10^{-7}	1.41×10^{-6}
Cl	3.75×10^{-7}	1.34×10^{-6}	3.75×10^{-7}	1.34×10^{-6}
SiCl	2.60×10^{-7}	1.86×10^{-8}	2.60×10^{-7}	1.86×10^{-8}
Si	5.23×10^{-8}	1.05×10^{-9}	5.23×10^{-8}	1.05×10^{-9}
Na_2	2.40×10^{-8}	1.88×10^{-9}	2.40×10^{-8}	1.88×10^{-9}
CO_2	3.21×10^{-10}	7.99×10^{-7}	0	0
SiO_2	6.33×10^{-11}	6.33×10^{-11}	0	0
Cl_2	1.64×10^{-11}	2.09×10^{-10}	1.64×10^{-11}	2.09×10^{-10}
NO	1.34×10^{-13}	9.22×10^{-13}	0	0
NaO	7.72×10^{-15}	1.53×10^{-14}	0	0
SiC	2.60×10^{-16}	2.60×10^{-16}	2.60×10^{-16}	2.60×10^{-16}
N_2O	7.09×10^{-18}	4.72×10^{-17}	0	0
O_2	1.11×10^{-21}	5.52×10^{-20}	0	0
NO_2	3.99×10^{-26}	1.93×10^{-24}	0	0
Condensed				
SiC	1	1	1	1
SiO_2	1	1	0	0
Si	1	0.0200578	1	0.0200578
NaCl	1	1	1	1
$Na_2Si_2O_5$	0.00050626	0.00028053	0	0
Na_2SiO_3	5.86×10^{-5}	3.25×10^{-5}	0	0
C	0.0200578	1	0.0200578	1

TABLE IV.—CALCULATED ACTIVITIES FOR GASEOUS AND CONDENSED SPECIES WITH DIFFERENT CONDENSED PHASES PRESENT AT 1400 °C (2552 °F)

Species	SiC + NaCl + SiO_2 + Si	SiC + NaCl + SiO_2 + C	SiC + NaCl + Si	SiC + NaCl + C
N_2	0.558418	0.456632	0.563253	0.564219
NaCl	0.302584	0.2637	0.304386	0.305491
Na_2Cl_2	0.126453	0.0960413	0.127964	0.1288954
SiO	0.00722118	0.00125192	0	0
Na	0.00292722	0.00084934	0.00293889	0.00093826
$SiCl_2$	0.00142103	0.00038532	0.00142662	0.00042375
CO	0.0009437	0.181105	0	0
$SiCl_3$	2.60×10^{-5}	2.12×10^{-5}	2.62×10^{-5}	2.45×10^{-5}
Cl	1.74×10^{-6}	5.23×10^{-6}	1.75×10^{-6}	5.49×10^{-6}
SiCl	1.62×10^{-6}	1.46×10^{-7}	1.62×10^{-6}	1.53×10^{-7}
$SiCl_4$	9.94×10^{-7}	2.43×10^{-6}	1.00×10^{-6}	2.94×10^{-6}
Si	4.00×10^{-7}	1.20×10^{-8}	4.00×10^{-7}	1.20×10^{-8}
Na_2	1.53×10^{-7}	1.29×10^{-8}	1.54×10^{-7}	1.57×10^{-8}
CO_2	5.12×10^{-9}	5.67×10^{-6}	0	0
SiO_2	8.71×10^{-10}	8.71×10^{-10}	0	0
Cl_2	1.12×10^{-10}	1.01×10^{-9}	1.12×10^{-10}	1.11×10^{-9}
NO	1.39×10^{-12}	7.24×10^{-12}	0	0
NaO	1.79×10^{-13}	3.00×10^{-13}	0	0
SiC	9.04×10^{-15}	9.04×10^{-15}	9.04×10^{-15}	9.04×10^{-15}
N_2O	6.10×10^{-17}	2.88×10^{-16}	0	0
O_2	7.20×10^{-20}	2.40×10^{-18}	0	0
NO_2	2.56×10^{-24}	7.69×10^{-23}	0	0
Condensed				
SiC	1	1	1	1
Si	1	0.0300563	1	0.0300563
SiO_2	1	1	0	0
NaCl	0.948752	0.826832	0.954403	0.957867
$Na_2Si_2O_5$	0.00109306	0.0005308	0	0
Na_2SiO_3	0.00013177	6.40×10^{-5}	0	0
C	0.03000563	1	0.0300563	1

TABLE V.—CALCULATED ACTIVITIES FOR GASEOUS AND CONDENSED SPECIES WITH DIFFERENT CONDENSED PHASES PRESENT AT 1500 °C (2732 °F)

Species	SiC + NaCl + SiO_2 + Si	SiC + NaCl + SiO_2 + C	SiC + NaCl + Si	SiC + NaCl + C
N_2	0.520544	0.389022	0.539248	0.540842
NaCl	0.360333	0.288156	0.370286	0.373165
Na_2Cl_2	0.0771595	0.0493442	0.0814809	0.0827529
SiO	0.0275961	0.00762716	0	0
Na	0.00589145	0.00217786	0.00599984	0.00217104
CO	0.0055439	0.262586	0	0
$SiCl_2$	0.00286999	0.00102598	0.00292221	0.00100409
$SiCl_3$	4.49×10^{-5}	3.47×10^{-5}	4.61×10^{-5}	4.41×10^{-5}
SiCl	7.08×10^{-6}	1.17×10^{-6}	7.14×10^{-6}	8.81×10^{-7}
Cl	5.91×10^{-6}	1.28×10^{-5}	5.97×10^{-6}	1.66×10^{-5}
Si	2.43×10^{-6}	1.86×10^{-7}	2.43×10^{-6}	1.08×10^{-7}
$SiCl_4$	1.19×10^{-6}	1.99×10^{-6}	1.23×10^{-6}	3.28×10^{-6}
Na_2	4.44×10^{-7}	6.07×10^{-8}	4.61×10^{-7}	6.04×10^{-8}
CO_2	6.20×10^{-8}	1.06×10^{-5}	0	0
SiO_2	8.86×10^{-9}	8.86×10^{-9}	0	0
Cl_2	4.61×10^{-10}	2.16×10^{-9}	4.69×10^{-10}	3.64×10^{-9}
NO	1.24×10^{-11}	3.87×10^{-11}	0	0
NaO	2.13×10^{-12}	2.85×10^{-12}	0	0
SiC	2.10×10^{-13}	2.10×10^{-13}	2.10×10^{-13}	2.10×10^{-13}
N_2O	5.18×10^{-16}	1.40×10^{-15}	0	0
O_2	2.95×10^{-18}	3.86×10^{-17}	0	0
NO_2	1.15×10^{-22}	1.31×10^{-21}	0	0
Condensed				
SiC	1	1	1	1
Si	1	0.0442988	1	0.0442988
SiO_2	1	1	0	0
NaCl	0.570859	0.456512	0.586626	0.591188
$Na_2Si_2O_5$	0.00117705	0.00058196	0	0
Na_2SiO_3	0.00014994	7.41×10^{-5}	0	0
C	0.0442988	1	0.0442988	1

TABLE VI.—CALCULATED ACTIVITIES FOR GASEOUS AND CONDENSED SPECIES WITH DIFFERENT CONDENSED PHASES PRESENT AT 1600 °C (2912 °F)

Species	SiC + NaCl + SiO_2 + Si	SiC + NaCl + SiO_2 + C	SiC + NaCl + Si	SiC + NaCl + C
N_2	0.457521	0.361458	0.52122	0.523599
NaCl	0.370224	0.304023	0.413905	0.420039
SiO	0.0904799	0.043057	0	0
Na_2Cl_2	0.0384404	0.1259221	0.0480464	0.0494808
CO	0.0277116	0.25715	0	0
Na	0.010414	0.00559088	0.0112201	0.00459793
$SiCl_2$	0.00508322	0.00269329	0.00547338	0.00215791
$SiCl_3$	6.73×10^{-5}	5.45×10^{-5}	7.52×10^{-5}	7.34×10^{-5}
SiCl	2.57×10^{-5}	8.91×10^{-6}	2.67×10^{-5}	4.25×10^{-6}
Cl	1.72×10^{-5}	2.62×10^{-5}	1.78×10^{-5}	4.41×10^{-5}
Si	1.22×10^{-5}	2.76×10^{-6}	1.22×10^{-5}	7.82×10^{-7}
$SiCl_4$	1.25×10^{-6}	1.55×10^{-6}	1.45×10^{-6}	3.51×10^{-6}
Na_2	1.03×10^{-6}	2.98×10^{-7}	1.20×10^{-6}	2.01×10^{-7}
CO_2	5.94×10^{-7}	1.16×10^{-5}	0	0
SiO_2	7.01×10^{-8}	7.01×10^{-8}	0	0
Cl_2	1.55×10^{-9}	3.63×10^{-9}	1.67×10^{-9}	1.02×10^{-8}
NO	8.49×10^{-11}	1.59×10^{-10}	0	0
NaO	1.80×10^{-11}	2.03×10^{-11}	0	0
SiC	3.46×10^{-12}	3.46×10^{-12}	3.46×10^{-12}	3.46×10^{-12}
N_2O	3.29×10^{-15}	5.47×10^{-15}	0	0
O_2	8.19×10^{-17}	3.62×10^{-16}	0	0
NO_2	3.39×10^{-21}	1.33×10^{-20}	0	0
Condensed				
Si	1	0.0642883	1	0.0642883
SiC	1	1	1	1
SiO_2	1	1	0	0
NaCl	0.32423	0.266253	0.362484	0.367855
$Na_2Si_2O_5$	0.00109197	0.00066137	0	0
Na_2SiO_3	0.00014874	9.01×10^{-5}	0	0
C	0.0642883	1	0.0642883	1

TABLE VII.—CALCULATED ACTIVITIES FOR GASEOUS AND CONDENSED SPECIES WITH DIFFERENT CONDENSED PHASES PRESENT AT 1700 °C (3092 °F)

Species	SiC + NaCl + SiO_2 + Si	SiC + NaCl + SiO_2 + C	SiC + NaCl + Si	SiC + NaCl + C
N_2	0.311134	0.272915	0.50861	0.511961
NaCl	0.275056	0.24449	0.434888	0.445956
SiO	0.260651	0.203483	0	0
CO	0.1206224	0.253526	0	0
Na	0.0144191	0.0113123	0.0195785	0.0090755
Na_2Cl_2	0.0108282	0.00855532	0.0270688	0.0284641
$SiCl_2$	0.00704177	0.00550906	0.00954812	0.004297
SiCl	7.46×10^{-5}	5.15×10^{-5}	8.68×10^{-5}	1.77×10^{-5}
$SiCl_3$	7.32×10^{-5}	6.49×10^{-5}	0.00011563	0.00011512
Si	5.17×10^{-5}	3.15×10^{-5}	5.17×10^{-5}	4.75×10^{-6}
Cl	4.07×10^{-5}	4.62×10^{-5}	4.74×10^{-5}	0.00010496
CO_2	4.67×10^{-6}	1.26×10^{-5}	0	0
Na_2	1.52×10^{-6}	9.34×10^{-7}	2.80×10^{-6}	6.01×10^{-7}
$SiCl_4$	9.07×10^{-7}	9.11×10^{-7}	1.67×10^{-6}	3.67×10^{-6}
SiO_2	4.48×10^{-7}	4.48×10^{-7}	0	0
Cl_2	3.83×10^{-9}	4.91×10^{-9}	5.19×10^{-9}	$2.54.\times10^{-8}$
NO	4.20×10^{-10}	5.04×10^{-10}	0	0
NaO	9.95×10^{-11}	1.00×10^{-10}	0	0
SiC	4.28×10^{-11}	4.28×10^{-11}	4.28×10^{-11}	4.28×10^{-11}
N_2O	1.33×10^{-14}	1.50×10^{-14}	0	0
O_2	1.64×10^{-15}	2.68×10^{-15}	0	0
NO_2	6.22×10^{-20}	9.56×10^{-20}	0	0
Condensed				
Si	1	0.091961	1	0.091961
SiC	1	1	1	1
SiO_2	1	1	0	0
NaCl	0.143584	0.127628	0.227019	0.232796
$Na_2Si_2O_5$	0.00068369	0.00053903	0	0
Na_2SiO_3	0.00010049	7.92×10^{-5}	0	0
C	0.091961	1	0.091961	1

TABLE VIII.—CALCULATED DIAMETERS FOR MOLECULAR SPECIES

Species	Calculated diameter, (A)
Ar	3.542
Cl	3.613
O_2	3.467
N_2	3.798
CO	3.690
SiO	3.374
SiCl	3.748
$SiCl_2$	[a]4.491
$SiCl_3$	[a]5.234
$SiCl_4$	5.977

[a]Estimated by analogy to other species; linear interpolation.

TABLE IX.—CALCULATED MEAN FREE PATHS FOR $SiCl_2$ IN N_2

Partial pressure (atm) N_2	Calculated mean free path (μm)					
	1200 °C	1300 °C	1400 °C	1500 °C	1600 °C	1700 °C
0.01	37.2	39.7	42.3	44.8	47.3	49.8
0.07	5.33	5.7	6.0	6.4	6.80	7.1

TABLE X.—CALCULATED DIFFUSIVITY FOR $SiCl_2$ IN N_2

Total pressure (atm)	Calculated diffusivity (cm^2/s)					
	1200 °C	1300 °C	1400 °C	1500 °C	1600 °C	1700 °C
0.01	73.9	81.6	89.5	97.6	106.0	114.6
0.07	10.6	11.7	12.8	13.9	15.1	16.4

TABLE XI.—CALCULATED PARABOLIC RATE CONSTANTS k_p FOR PINHOLE GROWTH

Total pressure (atm)	Calculated parabolic constants k_p (cm^2/s)					
	1200 °C	1300 °C	1400 °C	1500 °C	1600 °C	1700 °C
0.01	4.33×10^{-7}	1.88×10^{-6}	6.89×10^{-6}	1.67×10^{-5}	3.72×10^{-5}	7.59×10^{-5}
0.07	6.19×10^{-8}	2.68×10^{-7}	9.85×10^{-7}	2.39×10^{-6}	5.31×10^{-6}	1.08×10^{-5}

Figure 1.—Electron micrograph of a polished cross section of the oxidation protected RCC material.

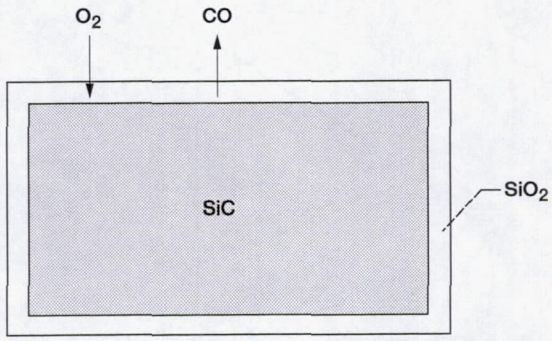

Figure 2.—Schematic for SiO_2 formation on SiC.

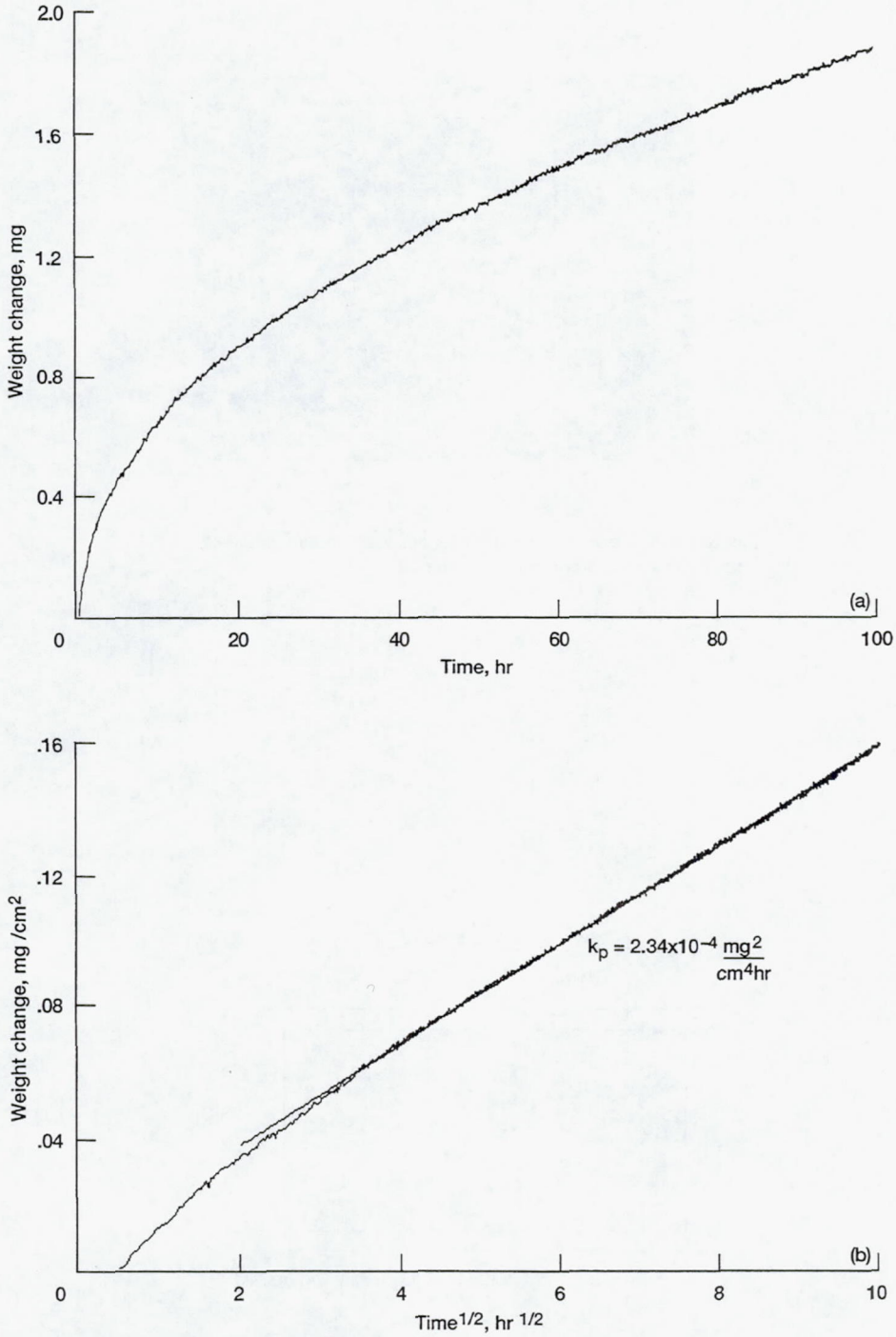

Figure 3.—Parabolic growth curve for SiO_2 forming on SiC at 1300 K, 1 atm oxygen. The parabolic rate constant is extracted from the lower plot.

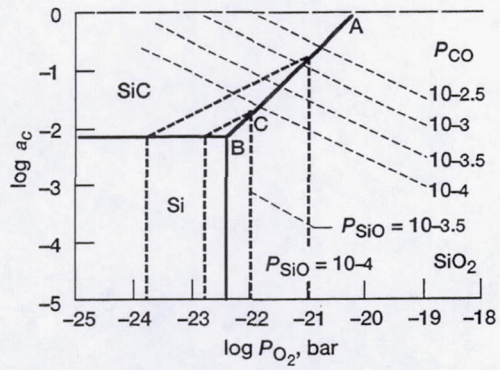

Figure 4.—Stability diagram for Si-C-O at 1500 K.[5]

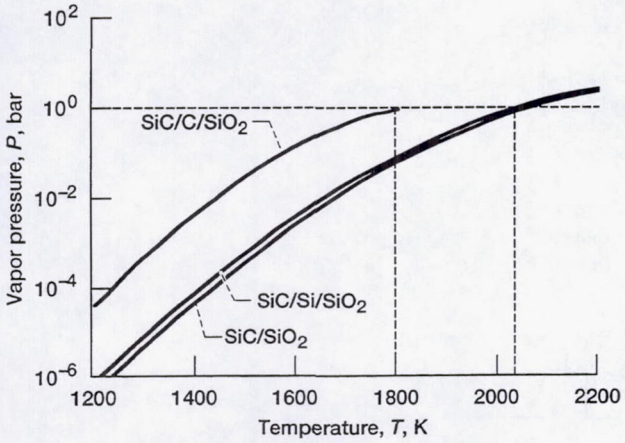

Figure 5.—Total vapor pressure from CO(g) and SiO(g) for carbon saturated SiC and SiO_2, silicon saturated SiC and SiO_2, and SiC and SiO_2 forming SiO and CO in a 3:1 molar ratio.[5]

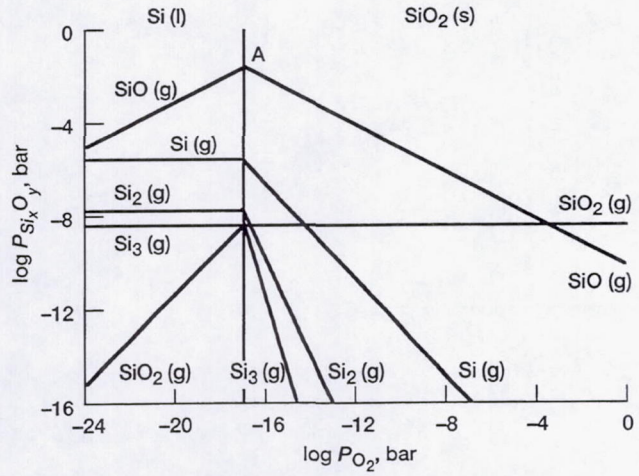

Figure 6.—Volatility diagram for the Si-O system at 1800 K (ref 10).

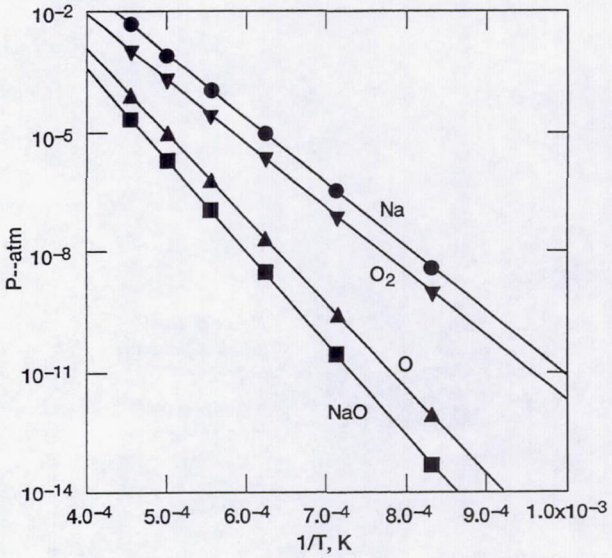

Figure 7.—Vapor species over $Na_2O.2$ (SiO_2) in vacuum as calculated via a free energy minimization computer code.

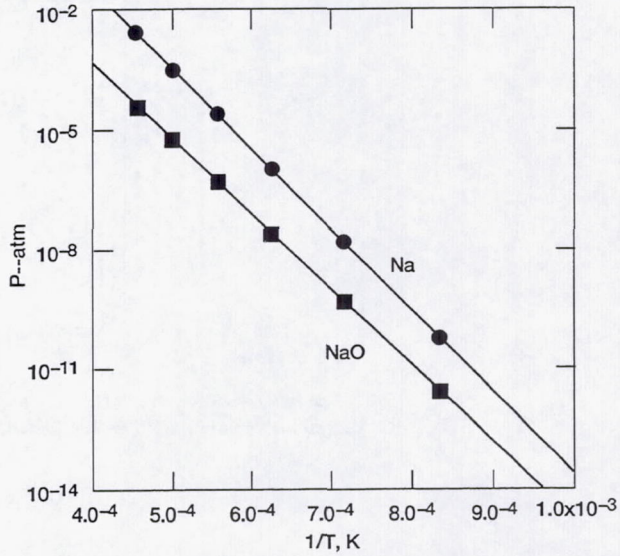

Figure 8.—Vapor species over $Na_2O.2$ (SiO_2) in .01 atm oxygen as calculated via a free energy minimization computer code.

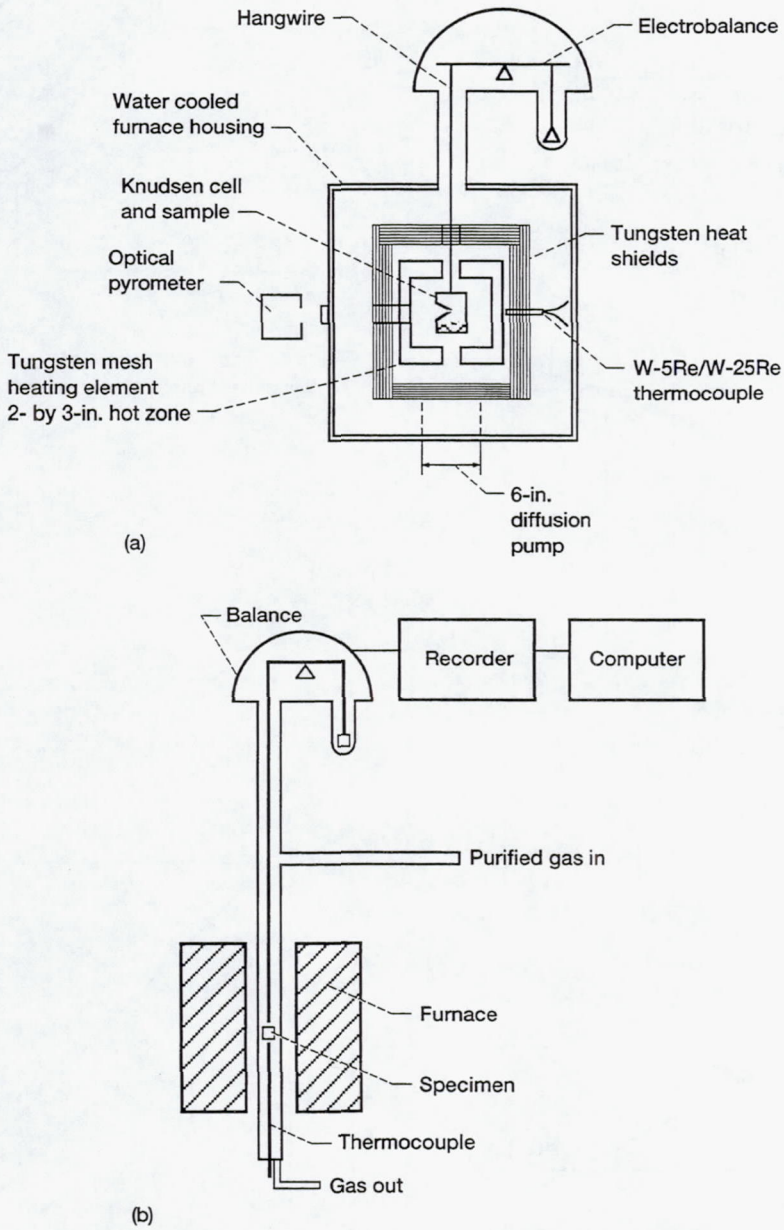

Figure 9.—Schematic of balance apparatus for measuring vaporization rates.
(a) Into a vacuum. (b) Into a gas atmosphere.

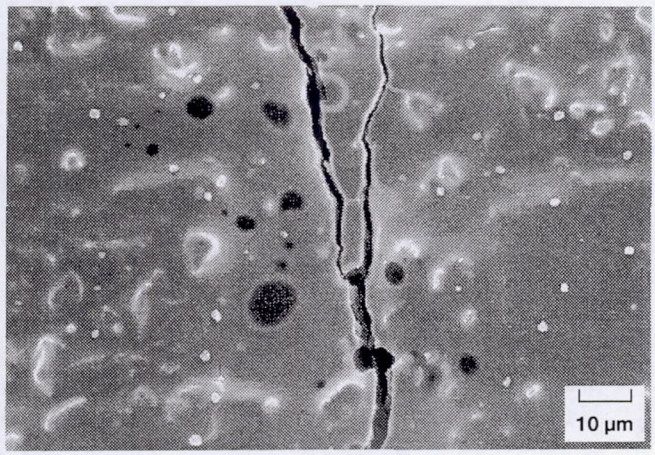

Figure 10.—Photomicrograph of thermally shocked RCC material, showing cracks in coating.

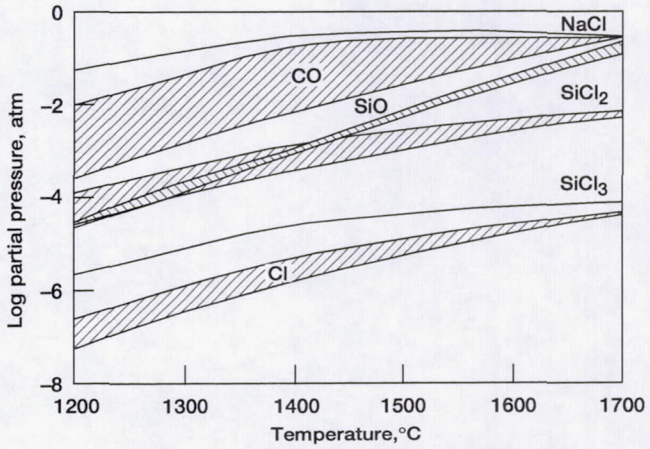

Figure 12.—Plot of vapor pressures for volatile species in equilibrium with SiO_2 + SiC + NaCl (passive reaction).

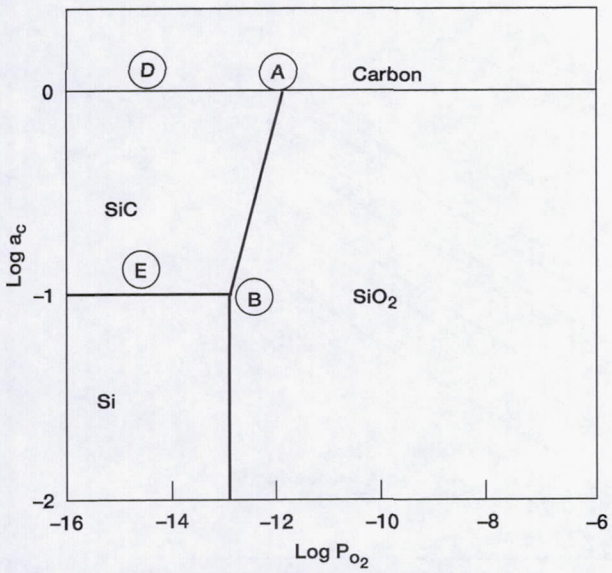

Figure 11.—Phase stability for SiC-C-O system at 2000 K (3141 °F).

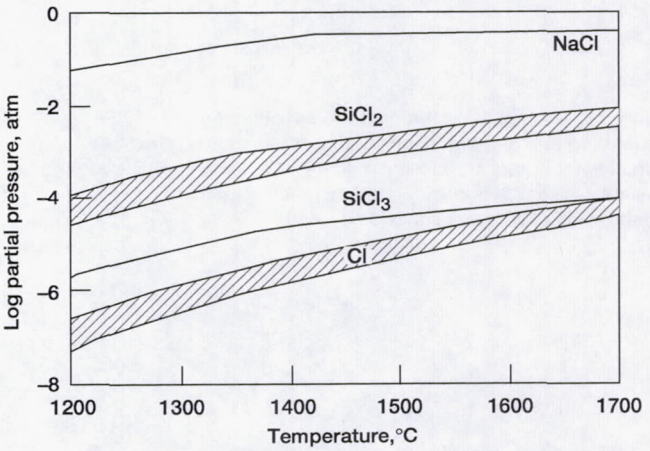

Figure 13.—Plot of vapor pressures for volatile species in equilibrium with SiC + NaCl (active reaction).

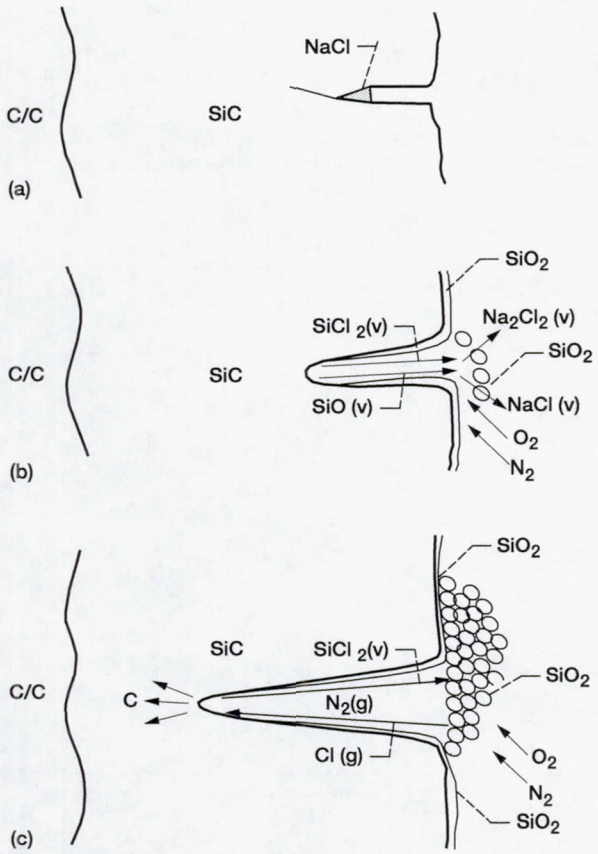

Figure 14.—Schematic representation of chloridation/oxidation reaction mechanism. (a) Contamination of surface cracks. (b) Transient passive reaction in a pinhole. (c) Steady-state active reaction with pinhole growth and fume deposition at external surface.

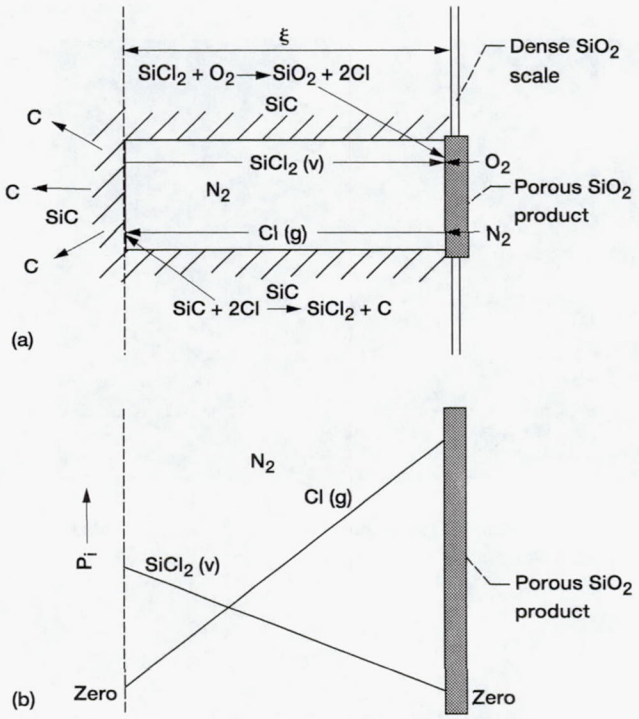

Figure 15.—Model for formation of a pinhole in a SiC coating on a C/C composite. (a) Schematic of a pinhole in a SiC coating on a C/C composite. (b) Partial pressure gradient in a pinhole.

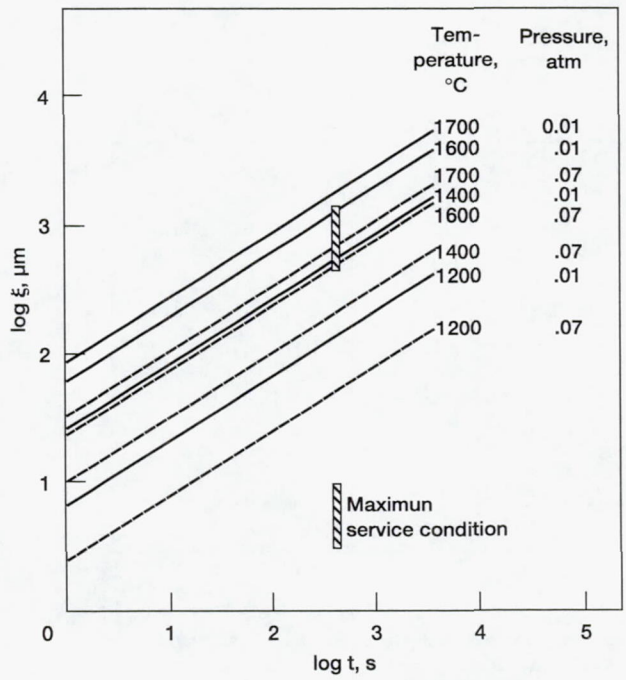

Figure 16.—Kinetics of formation of a pinhole in a SiC coating on a C/C composite.

APPENDIX A—ACTIVE TO PASSIVE AND PASSIVE TO ACTIVE TRANSITIONS

Wagner's paper on the active to passive transition (ref. 1) for silicon is the classic work in the field and can be adapted to SiC as is summarized here. Let us begin with a bare SiC surface. At very low oxygen pressures, a passive silica film does not form on an initially clean surface. Any oxygen molecules which do strike the surface react to form SiO(g) and CO(g) as follows:

$$SiC(s) + O_2(g) = SiO(g) + CO(g) \tag{A1}$$

The limitation in the arriving oxygen flux which permits and retains active reaction can arise from two limiting conditions: 1. A partial vacuum where the oxygen pressure approximates the total pressure, or 2. In the presence of a high pressure of an inert diluent gas, such that the dilute oxygen component can only reach the surface via gaseous diffusion through a stagnant boundary layer. Clearly, as long as SiC remains bare, the higher the oxygen flux, the more rapid this "active" reaction, as shown in figure (A1). The flux of Si loss in figure (A1) is simply proportional to the rate of oxygen arrival and reaction according to equation (A1). Obviously SiC(s) can be rapidly consumed under these conditions.

As the pressure of oxygen is increased, an oxygen arrival flux is reached at which a stable film of $SiO_2(s)$ will form, causing an abrupt drop in rate shown in figure (A1). In the literature (ref. 2) the condition to form a stable scale is the equilibrium between the three solid phases SiC, Si, and SiO_2, according to this expression:

$$2\ SiC(s) + SiO_2(s) = 3\ Si(c) + 2\ CO(g) \tag{A2}$$

To attain this equilibrium and a "passive" condition, we need a minimum CO(g) pressure, which can be calculated from the standard Gibbs free energy change for Reaction (A2). Thus once reaction (A1) generates enough CO pressure to achieve equilibrium for Reaction (A2), a stable SiO_2 scale is formed and the evaporation loss is virtually stifled. It is assumed that there are no kinetic barriers to these reactions. In its original publication the model presumed that the oxygen arrives at the surface by diffusion through some inert gas of much higher pressure, e.g. Ar, N_2, or He. The flux of oxygen molecules, J_{O_2}, striking a bare SiC surface may be written as follows:

$$J_{O_2} = [D_{O_2}/\delta_{O_2}]\ (P_{O_2}{}^{g} - P_{O_2}{}^{i})/RT \tag{A3}$$

Here δ is the boundary layer thickness, P^g the gas pressure in the bulk gas (far side of the boundary layer), P^i the pressure at the gas/SiC interface (generally assumed to be negligible), R the gas constant, and T the absolute temperature. The flux of CO(g) molecules, J_{CO}, leaving the surface is:

$$J_{CO} = [D_{CO}/\delta_{CO}]\ (P_{CO}{}^{i} - P_{CO}{}^{g})/RT \tag{A4}$$

Now $P_{CO}{}^{g}$ is assumed to be negligible. The fluxes are shown schematically in figure (A2). An analogous expression to (A4) can be written for the SiO flux. However we need not consider this, since it does not enter into the stable SiO_2/SiC equilibrium condition (equation (A2)). The fluxes can be equated according to equation (A1), $J_{O2} = J_{CO} = J_{SiO}$ and the result is:

$$P_{O_2} = (D_{CO}/D_{O_2})\ (\delta_{O_2}/\delta_{CO})\ P_{CO}{}^{i} \tag{A5}$$

This describes the steady state value for $P_{CO}{}^{i}$ for active oxidation. As Wagner pointed out, the ratio of boundary layer thicknesses can be approximated as $(D_{O_2}/D_{CO})^{1/2}$. Thus the necessary P_{O_2} for the active-to-passive transition becomes:

$$P_{O_2} \geq (D_{CO}/D_{O_2})^{1/2}\ P_{CO}{}^{eq} \tag{A6}$$

where $P_{CO}{}^{eq}$ is the equilibrium CO pressure calculated for Reaction (A2). The ratio, D_{CO}/D_{O_2} (as inferred from the molecular diameters of table VIII in the main text) is close to one. A plot of the predicted active-to-passive transition temperatures is shown in figure (A3). Measured values are within an order of magnitude of this and indicate the proper temperature dependence (ref. 2).

Suppose, however, that one starts with a passive $SiO_2(s)$ scale and the oxygen pressure is gradually reduced. At what point does the scale become unstable and active oxidation occur? Clearly, the above criterion does not hold and we must invoke a new criterion, which leads to the observed hysteresis, as indicated in figure (A1).

The factors which lead to the breakdown of passive $SiO_2(s)$ need to be identified. Note that for this analysis, any consideration of a NaCl deposit is avoided. We have an oxygen flux striking the surface, which contributes to scale growth. We also have SiO(g), $SiO_2(g)$, and $O_2(g)$ fluxes involved in the following vaporization processes:

$$SiO_2(s) = SiO(g) + 1/2\ O_2(g) \tag{A7}$$

$$SiO_2(s) = SiO_2(g) \tag{A8}$$

At low oxygen partial pressures, reaction (A7) dominates (ref. 3) and we can ignore the flux of $SiO_2(g)$. The flux of $O_2(g)$ is given by:

$$J_{O_2} = [D_{O_2}/\delta_{O_2}]\ (P_{O_2}^{g} - P_{O_2}^{s})/RT \tag{A9}$$

Here the terms have the same definitions as given previously, with $P_{O_2}^{s}$ being the pressure of O_2 at the surface. In this instance, neither $P_{O_2}^{g}$ or $P_{O_2}^{s}$ can be neglected. The flux of SiO(g) leaving the surface is given as:

$$J_{SiO} = [D_{SiO}/\delta_{SiO}]\ (P_{SiO}^{s} - P_{SiO}^{g})/RT \tag{A10}$$

The two fluxes are shown schematically in figure (A4) and are related by the expression $J_{O_2} = 1/2\ J_{SiO}$. Now we can neglect P_{SiO}^{g} and express P_{SiO}^{s} in terms of P_{O2}^{s} via the equilibrium constant for Reaction (A7):

$$K = P_{SiO}^{s}(P_{O_2}^{s})^{1/2} \tag{A11}$$

Combining equations (A9) to (A11) and correlating the boundary layer thickness to diffusivities, as done previously, leads to:

$$2(P_{O_2}^{g} - P_{O_2}^{s}) = K\ (D_{SiO}/D_{O_2})^{1/2}/(P_{O_2}^{s})^{1/2} \tag{A12}$$

As explained by Wagner (ref. 1), the left-hand side of equation (A12) is proportional to the supply of oxygen and the right-hand side is proportional to the consumption of oxygen. A stable SiO_2 scale is maintained only when the oxygen supplied is equal to or greater than the amount consumed. The minimum $P_{O_2}^{g}$ for which the conditions of equation (A12) is met can be calculated by expressing equation (A12) as a function of $P_{O_2}^{g}$ and calculating the minimum for that expression:

$$f(P_{O_2}^{g}) = 2P_{O_2}^{s} + K\ (D_{SiO}/D_{O_2})^{1/2}/(P_{O_2}^{s})^{1/2} = 2\ P_{O_2}^{g} \tag{A13}$$

The minimum value is obtained by taking the derivative of equation (A13) with respect to $P_{O_2}^{s}$ and setting the resultant expression equal to zero:

$$P_{O_2}^{s} = (K/4)^{2/3}\ (D_{SiO}/D_{O_2})^{1/3} \tag{A14}$$

The value of $P_{O_2}^{g}$ can be calculated by combining equations (A14) and (A12):

$$P_{O_2}^{g} = 1/2\ [2/(4)^{2/3} + (4)^{1/3}]\ K^{2/3}\ (D_{SiO}/D_{O_2})^{1/3} \tag{A15}$$

This is the oxygen pressure at which active oxidation begins; such values have been plotted onto figure (A3) which shows the results of this calculation for a range of temperatures. Note the large difference between the active-to-passive and the passive-to-active transition points. Also, recall the outer layer on the RCC panels is likely to be a silica-satured sodium silicate, not pure silica. So these boundaries are only approximations.

Since the RCC panels start with a coating of $SiO_2(s)$, it is this lower transition pressure that induces active behavior that concerns us. Clearly the transition to true active oxidation is only expected at this extreme condition of very low pressure.

REFERENCES FOR APPENDIX A

1. C. Wagner, "Passivity during the Oxidation of Silicon at Elevated Temperatures," J. Appl. Phys. 29 [9], 1295 (1958).
2. E.A. Gulbransen and S.A. Jansson, "The High Temperature Oxidation, Reduction, and Volatilization Reactions of Silicon and Silicon Carbide," Oxid. Met. 4 [3], 181 (1972).
3. N.S. Jacobson, "High Temperature Durability Considerations for the HSCT Combustor," NASA TP–3162, 1992.

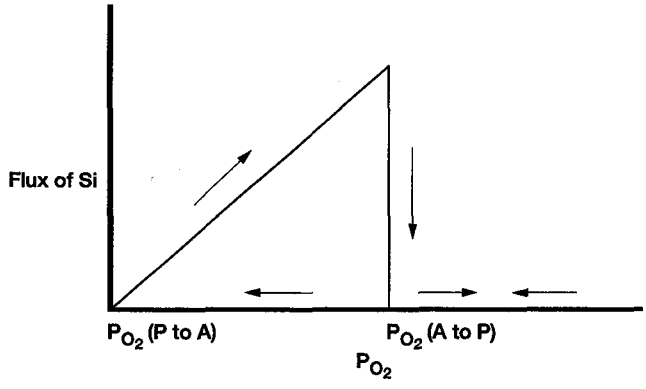

Figure A1.—Schematic showing active to passive and passive to active transitions as a function of $P(O_2)$.

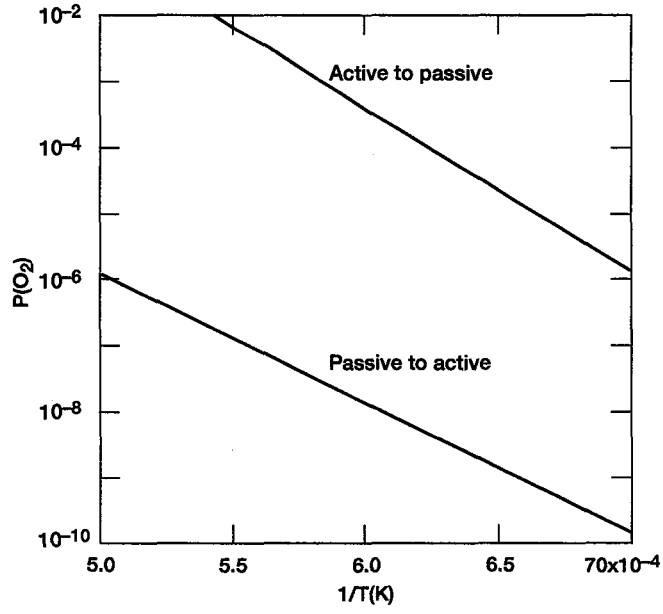

Figure A3.—Calculated active-to-passive and passive-to active transitions for SiC as a function of temperature.

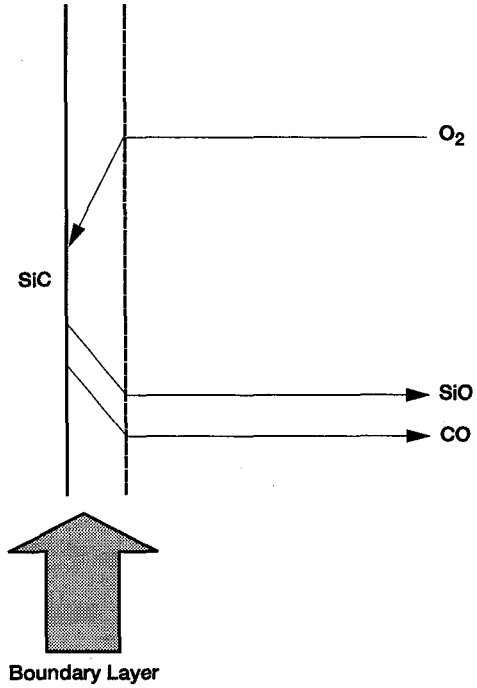

Figure A2.—Schematic showing diffusion of O_2, SiO, and CO through the boundary layer at a bare SiC surface. Boundary layers for each gas are shown as the same thickness due to close molecular weights.

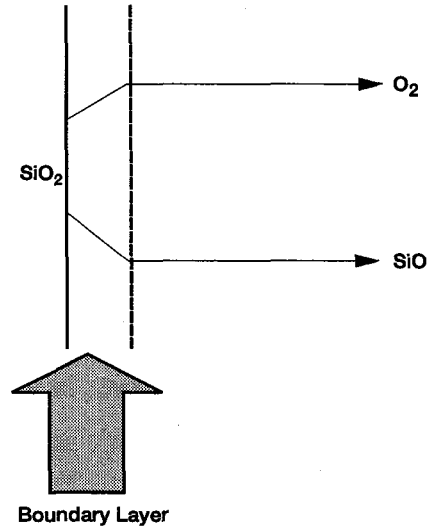

Figure A4.—Schematic showing diffusion of O_2 through the boundary layer away from SiO_2. Boundary layers for each gas are shown as the same thickness due to close molecular weights.

APPENDIX B—OXIDATION OF C/C BENEATH A SiC COATING CONTAINING PINHOLES

When pinholes form in a SiC coating, the underlying C/C composite substrate is exposed to an oxidizing environment through the pinholes, and oxidation of the carbon occurs. A calculation of the oxidation rate though a flawed SiC coating on the C/C composite is made in the following. Some parameters used are as follows:

(1) Thickness of the SiC coating: 20 to 40 mils (508 to 1016 μm)
(2) Diameter of the pinhole: 20 to 40 mils (508 to 1016 μm)
(3) Environment: 001 to 0.07 atm-air (pressure created by shock wave)
(4) Temperature: 1473 to 1973 K

The oxidation of C layers in composites has been reported in references 1 and 2, and a similar treatment for the oxidation of TaC is treated in reference 3. A modification of the model in reference 1 is employed for oxidation of a C/C composite underneath a pinhole in a SiC coating, as shown in figure (B1). The pinhole is filled with four gaseous species: inert N_2, the active oxidant O_2 from air, and the two oxidation products CO and CO_2. At the C/gas phase interface, the oxygen partial pressure is very low and the primary C oxidation product at very high temperature is CO. Under these conditions CO and O_2 cannot coexist. Hence we have two regions in the pore--one with O_2 and CO_2 and one with CO and CO_2. The CO forms by reaction of C with CO_2 at the base of coating, diffuses outward and at a more forward site in the pinhole, x_f, it is oxidized again to form CO_2. The CO_2 oxidation product diffuses both inward as an oxidant to oxidize C at $x = 0$ and outward as a product through the pinhole to the environment. The gas within the voids in C/C caused by oxidation through the pinhole is assumed to remain in equilibrium with pure C (virtually pure CO). The concentration (partial pressure) profiles of the gaseous species in the pinhole are shown in figure (B2). The two regions (I and II) are identified in the pinhole, as labelled in figure (B2). The concentration profiles and the rate of carbon oxidation can be obtained through analysis of the diffusion fluxes for the gaseous species in these two regions.

(I) Diffusivities of O_2, CO and CO_2 in N_2

To calculate the oxidation rate of carbon at the base of a pinhole, diffusivities for O_2, CO and CO_2 in N_2 are required. These diffusivities are calculated by the following equation (ref. 4):

$$D_{i-N_2} = (2/3)(k_B/\pi)^{3/2}[1/(2m_i) + 1/(2m_{N_2})]^{1/2}T^{3/2}/P_T/[(d_i + d_{N_2})/2]^2 \quad \text{(B1)}$$

where k_B is the Boltzmann constant, m_i the weight of species i per molecule, P_T the total pressure, T the absolute temperature, and d_i the diameter of species i. The calculated diffusivities are listed in table BI.

TABLE BI.—DIFFUSIVITIES (cm^2/s) OF O_2, CO AND CO_2 IN N_2*

Species, $d_i(A)^5$	O_2, 3.467		CO, 3.690		CO_2 3.941	
P(atm)	0.01	0.07	0.01	0.07	0.01	0.07
1473K	116.4	16.6	113.2	16.2	95.8	13.7
1573K	128.5	18.4	124.9	17.8	105.8	15.1
1673K	140.9	20.1	137.0	19.6	116.0	16.6
1773K	153.7	22.0	149.4	21.3	126.6	18.1
1873K	166.9	23.8	162.3	23.2	137.4	19.6
1973K	180.5	25.8	175.4	25.1	149.6	21.2

*Diameter of N_2 is 3.798 A (ref. 5).

(II) Mass Transport in Region I

In region I of figure B2, a steady-state mass transport calculation is provided as follows. The inward flux of O_2 is independent of distance in region I and given by:

$$J'_i = -D_i(dC_i/dx) + vC_i \tag{B2}$$

where D_i and C_i are the diffusivity and concentration of species i, and v is the local molar average velocity, which is defined as:

$$v = \Sigma(C_i v_i)/\Sigma C_i = \Sigma(J_i)/C_T \tag{B3}$$

where C_i, v_i, and J_i are the concentration, local molar velocity and the flux of species i, respectively, and C_T is the total concentration of gaseous species. The net flux of N_2 is zero in both the regions I and II because neither a sink nor a source for N_2 exists in the pinhole. The concentration and flux of CO are negligible in region I. From the mass balance, the inward flux of O_2 equals the outward flux of CO_2 in region I, i.e.,

$$J'_{O_2} = -J'_{CO_2} \tag{B4}$$

and by inserting equation (B4) into equation (B3), v is equal to zero. The concentration profiles for both O_2 and CO_2 are linear because of the constant dC_i/dx in equation (B2). From equation (B2) for O_2 and CO_2:

$$J'_{O_2} = -D_{O_2}C^{\circ}_{O_2}/(L - x_f) \tag{B5}$$

and

$$J'_{CO_2} = D_{CO_2}C^{*}_{CO_2}/(L - x_f) \tag{B6}$$

From equations (B4) and (B6),

$$C^{*}_{CO_2} = C^{\circ}_{O_2}\, D_{O_2}/D_{CO_2} \tag{B7}$$

where $C^{\circ}_{O_2}$ is the oxygen concentration at the external surface, and $C^{*}_{CO_2}$ is the CO_2 concentration at $x = x_f$. The concentration profiles for O_2 and CO_2 in region I are plotted in figure (B2).

(III) Mass Transport in Region II

From a mass balance, the following relations are obtained:

$$J''_{N_2} = 0 \tag{B8}$$

$$J''_{CO} = -2J''_{CO_2} \tag{B9}$$

and inserting equations (B8) and (B9) into equation (3) yields:

$$v = -J''_{CO_2}/C_T \tag{B10}$$

The flux of CO_2 in the region II is given by:

$$J''_{CO_2} = -D_{CO_2}(dC_{CO_2}/dx) - C_{CO_2}J''_{CO_2}/C_T \tag{B11}$$

Rearrangement of equation (B11) gives:

$$J''_{CO_2}dx = -[C_T D_{CO_2}/(C_T + C_{CO_2})]dC_{CO_2} \tag{B12}$$

Equation (B12) is integrated from $x = 0$ to x_f on the left-hand side and from $C_{CO_2} = C^{**}_{CO_2}$ to $C^{*}_{CO_2}$ on the right-hand side, where the superscript double star denotes the reaction side at $x = 0$. The result is:

$$J''_{CO_2} = -(C_T D_{CO_2}/x_f)\ln[(C_T + C^{*}_{CO_2})/(C_T + C^{**}_{CO_2})] \tag{B13}$$

Because $C^{**}_{CO_2}$ is much lower than $C^{*}_{CO_2}$, equation (B13) is simplified as:

$$J''_{CO_2} = -(C_T D_{CO_2}/x_f)\ln[1 + C^{*}_{CO_2}/C_T] = -(C_T D_{CO_2}/x_f)\ln[1 + C^{o}_{O_2} D_{O_2}/(C_T D_{CO_2})] \quad \text{(B14)}$$

A mass balance between CO and O_2 results in the following relation:

$$J''_{CO} = -2J'_{O_2} \quad \text{(B15)}$$

Combining equations (B9) and (B15) yields:

$$J'_{O_2} = J''_{CO_2} \quad \text{(B16)}$$

From equations (B5), (B14) and (B16),

$$-(C_T D_{CO_2}/x_f)\ln[1 + C^{o}_{CO_2} D_{O_2}/(C_T D_{CO_2})] = - C^{o}_{O_2} D_{O_2}/(L - x_f) \quad \text{(B17)}$$

Equation (B17) can be rearranged to give:

$$L/x_f = 1 + C^{o}_{O_2} D_{O_2}/(C_T D_{CO_2})/\ln[1 + C^{o}_{O_2} D_{O_2}/(C_T D_{CO_2})] \quad \text{(B18)}$$

According to equation (B11), D_{O_2}/D_{CO_2} is independent of temperature. For a system with a given $C^{o}_{O_2} C_T$, (i.e., P_{O_2}/P_T) in the environment, the ratio of the lengths of the regions I to II is a constant. For the environment of air, P_{O_2}/P_T is 0.21 and the calculated value for L/x_f is 2.123.

Similarly, the flux of CO in the region II can be obtained as follows:

$$J''_{CO} = -D_{CO}(dC_{CO}/dx) + C_{CO}(J''_{CO} + J''_{CO_2})/C_T \quad \text{(B19)}$$

From equation (B9), equation (B19) can be rewritten as:

$$J''_{CO}dx = -[2C_T D_{CO}/(2C_T - C_{CO})]dC_{CO} \quad \text{(B20)}$$

Integration of equation (B20) from $x = 0$ to x_f and $C_{CO} = C^{**}_{CO}$ to C^{*}_{CO} yields:

$$J''_{CO} = -(2C_T D_{CO}/x_f)\ln[(2C_T - C^{**}_{CO})/(2C_T - C^{*}_{CO})] \quad \text{(B21)}$$

Because C^{*}_{CO} is much less than C^{**}_{CO}, equation (B21) is simplified as:

$$J''_{CO} = -(2C_T D_{CO}/x_f)\ln[1 - C^{**}_{CO})/(2C_T)] \quad \text{(B22)}$$

By combining equations (B9), (B14) and (B22), C^{*}_{CO} is obtained as:

$$C^{**}_{CO} = 2C_T\{1 - [1 + C^{o}_{O_2} D_{O_2}/(C_T D_{CO_2})]^{-D_{CO2}/D_{CO}}\} \quad \text{(B23)}$$

The concentration profiles of both CO and CO_2 are nonlinear in the region II, as shown in figure (B2).

(IV) Oxidation Rate for C/C

The weight-loss rate due to C/C oxidation per unit pinhole area in a SiC coating is related to the flux of CO_2, according to a mass balance, as follows:

$$dW_C/dt = M_C J'_{CO_2} = M_C J'_{O_2} = M_C C^{o}_{O_2} D_{O_2}/(L - x_f) = M_C P_{O_2} D_{O_2}/[(L - x_f)RT] \quad \text{(B24)}$$

The calculated weight-losses per cm^2 of pinhole area are the same for P = 0.01 and 0.07 atm, as plotted in figure (B3). The weight-loss rate per pinhole is given by:

$$W_C = r^2\pi(dW_C/dt) = r^2\pi M_C J'_{O_2} = r^2\pi M_C C^o_{O_2} D_{O_2}/(L - x_f) \quad (B25)$$

where r is the radius of the pinhole. The calculated results for pinhole of diameters of 20 to 40 mils at temperatures of 1473 and 1973 K are shown in figures (B4) and (B9).

If a hemispherical cavity is assumed to grow at the bottom of a pinhole, the weight loss rate of C can be converted to the size of a cavity as follows:

$$W_C = d_C(dV/dt) = d_C[d(2\pi r_C^3/3)dt] \quad (B26)$$

where V is the volume of the cavity, d_C the density of C/C, and r_C the radius of the cavity. Integration of equation (B26) yields:

$$r_c = [3W_C t/(2\pi d_C)]^{1/3} = \{3r^2 M_C P_{O_2} D_{O_2} t/[RT(L - x_f)(2d_C)]\}^{1/3} \quad (B27)$$

The density of C is in a range of 1.8 to 2.25 g/cm^3 (ref. 6), and 2 g/cm^3 is chosen in the following calculation. The calculated results are plotted in figures (B10) and (B11) for temperatures of 1473 to 1973 K and different pinhole sizes. The size of a cavity formed is strongly dependent on the size of a pinhole, and weakly dependent on temperature, as shown in figure (B10).

(V) Discussion

(i) Ratio of L/x_f

The ratio of L/x_f is very important to the oxidation rate of C because the oxidation rate is proportional to the flux of O_2, which is inversely proportational to $L - x_f$. As analyzed in the section III, the ratio of L/x_f is independent of both temperature and total pressure if P_{O_2}/P_T is fixed. But the ratio P_{O_2}/P_T plays an important role in the oxidation rate by changing the ratio of L/x_f. At a given temperature and a given P_{O_2}, the ratio of L/x_f decreases with increasing P_T, according to equation (B18). Two extreme cases are discussed in the following:

(a) $P_T >> P_{O_2}$

In this case, $L/x_f = 2$ because $\ln[1 + C^o_{O_2} D_{O_2}/(C_T D_{CO_2})]$ is approximately equal to $C^o_{O_2} D_{O_2}/(C_T D_{CO_2})$ in equation (B18). Also, minimum value of L/x_f is 2.

(b) $P_T = P_{O_2}$

This is a case of oxidation in a pure O_2 environment. Equation (B18) becomes:

$$L/x_f = (1 + D_{O_2} D_{CO_2})/\ln(1 + D_{O_2}/D_{CO_2}) = 1 + 1/\ln 2 = 2.44 \quad (B28)$$

if D_{O_2} (in CO_2) is assumed equal to D_{CO_2} (in CO), which is the maximum value of L/x_f.

(ii) Effect of Total Pressure on Oxidation Rate

The diffusivity of gaseous species is inversely proportional to P_T, as shown in equation (B1). For a system with a given P_{O_2} at a given temperature, the oxidation rate is inversely proportional to P_T, the same as D_{O_2}.

Because $C^o_{O_2}$ is proportional P_{O_2} and D_{O_2} is inversely proportional to P_T, the product of $C_{O_2} D_{O_2}$ is unchanged if P_{O_2}/P_T is fixed. For a given P_{O_2}/P_T and a given temperature, the oxidation rate is unchanged even if both P_{O_2} and P_T are changed.

(iii) Temperature Effect on Oxidation Rate

According to the above calculation, the ratio of L/x_f is independent of temperature. For a system with a given P_{O_2}/P_T, the oxidation rate is proportional to D_{O_2}, which is proportional $T^{1.5}$. In other words, the oxidation rate for a given pinhole population increases with the square root of temperature if the ratio of P_{O_2}/P_T is fixed. The growth rate of a cavity in C/C at the bottom of a pinhole is proportional to $T^{1/6}$, according to equation (B27), and as temperature increases from 1473 to 1973 K, the growth rate only increases 5 percent. The growth rate is virtually dependent on the size of a cavity if the ratio of P_{O_2}/P_T is fixed.

REFERENCES

1. J. Bernstein and T.B. Koger, J. Electrochem. Soc., 135, 2086–90, 1988.
2. A.J. Eckel, J.D. Cawley, and T.A. Parthasarathy, "Oxidation of a Continuous Carbon Phase in a Non-reactive Matrix," J. Amer. Cer. Soc., in press.
3. G.R. Holcolm and G.R. St. Pierre, Oxid. Metals, 40, 109–118, (1993).
4. G.H. Geiger and D.R. Poirier, Transport Phenomena in Metallurgy, Addison-Welsey Publication Company, Reading, Massachusetts, 1973.
5. R.A. Svehla, "Estimated Viscosities and Thermal Conductivities of Gases at High Temperatures," NASA TR–132.
6. CRC Handbook of Chemistry and Physics, 52nd ed., R.C. Weast, ed., The Chemical Rubber Co., Cleveland, Ohio, 1971, p. B–79.

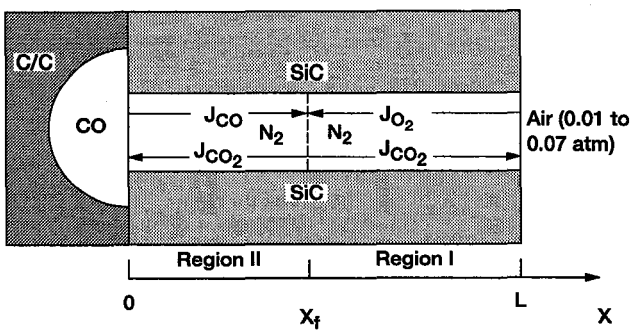

Figure B1.—Model for oxidation of C/C composite at the bottom of a pinhole in a SiC coating.

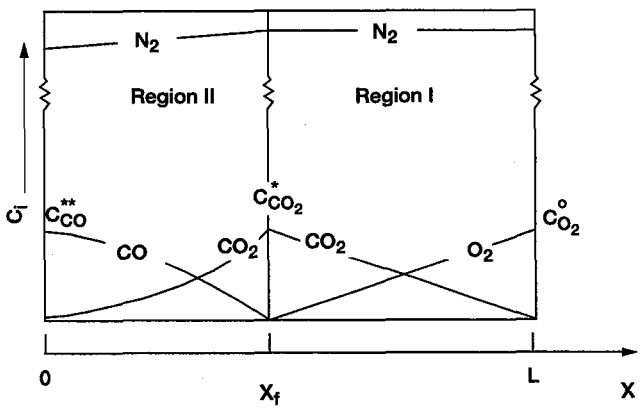

Figure B2.—Concentration profiles of O_2, CO, CO_2 and N_2 in a pinhole where $C_i = P_i/RT$.

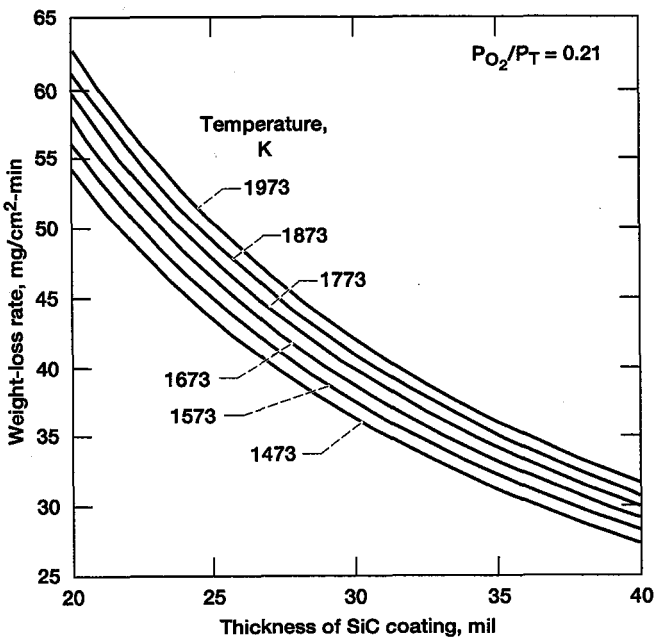

Figure B3.—Weight-loss rate per cm^2 of pinhole area in a SiC coating on a C/C composite at temperature 1473 - 1973 K and $P_{O_2}/P_T = 0.21$.

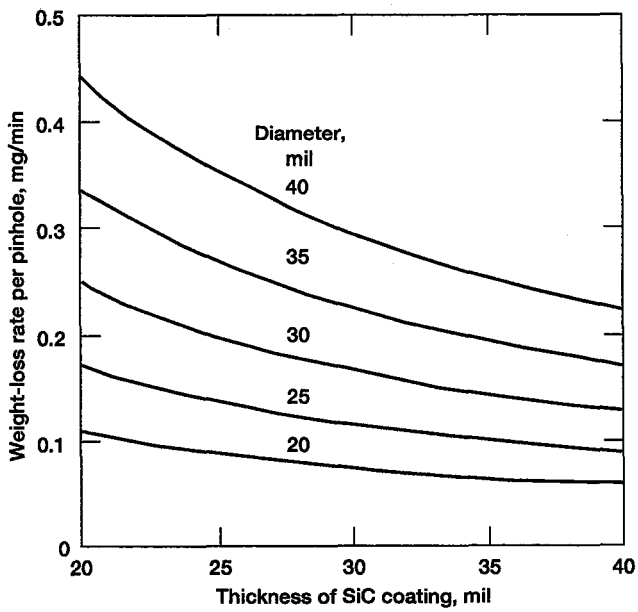

Figure B4.—Weight-loss rate per pinhole at 1473 K and $P_{O_2}/P_T = 0.21$.

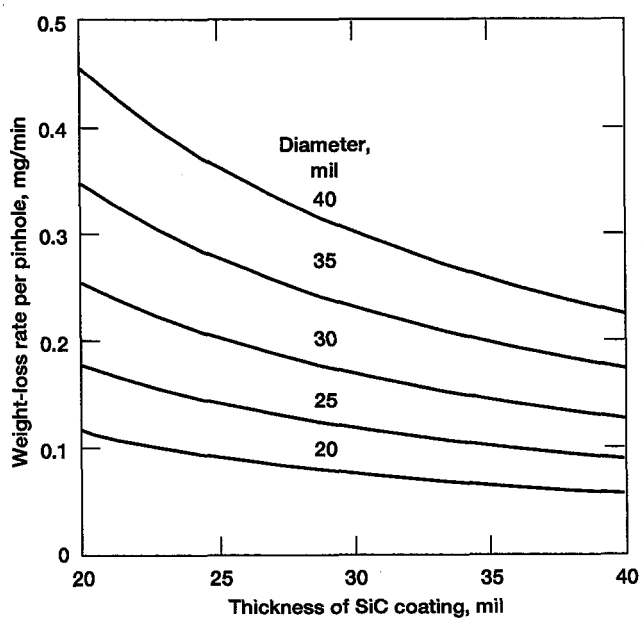

Figure B5.—Weight-loss rate per pinhole at 1573 K and $P_{O_2}/P_T = 0.21$.

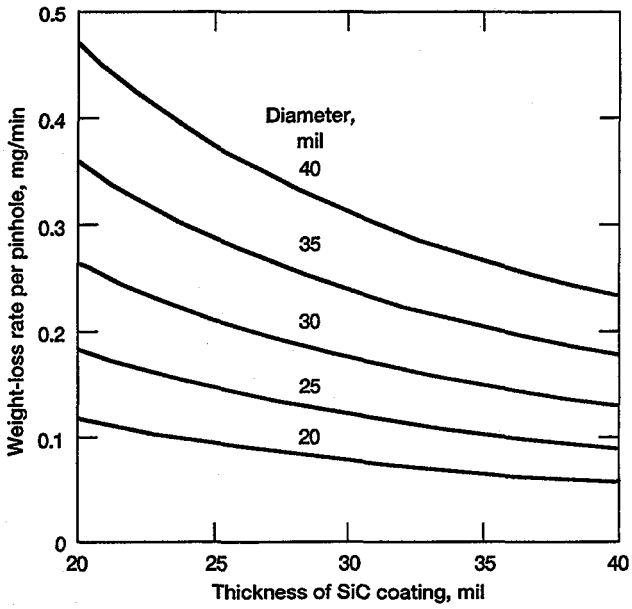

Figure B6.—Weight-loss rate per pinhole at 1673 K and $P_{O_2}/P_T = 0.21$.

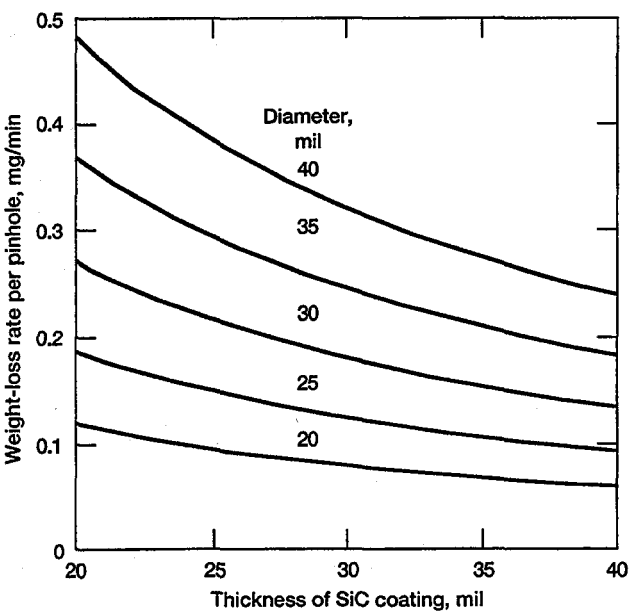

Figure B7.—Weight-loss rate per pinhole at 1773 K and $P_{O_2}/P_T = 0.21$.

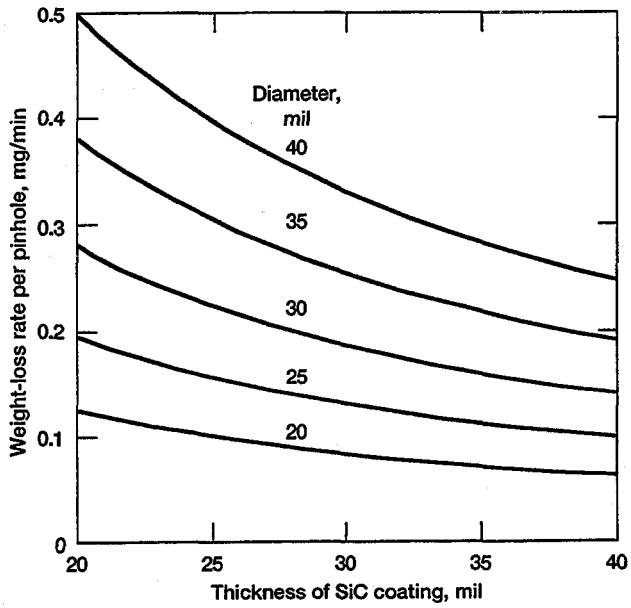

Figure B8.—Weight-loss rate per pinhole at 1873 K and $P_{O_2}/P_T = 0.21$.

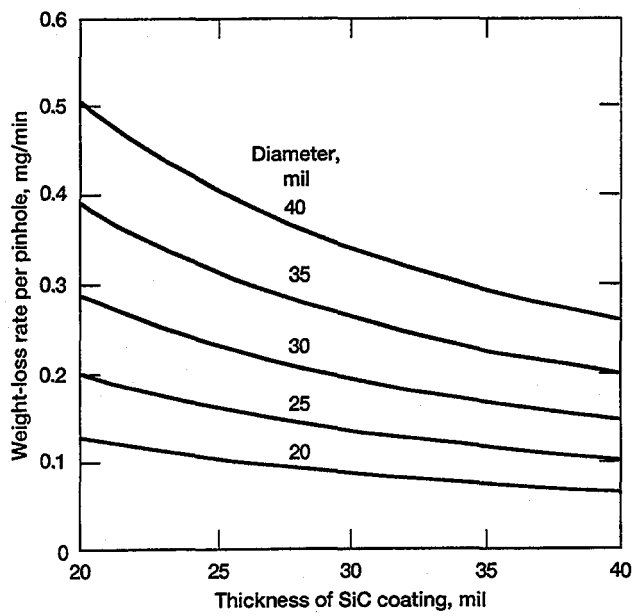

Figure B9.—Weight-loss rate per pinhole at 1973 K and $P_{O_2}/P_T = 0.21$.

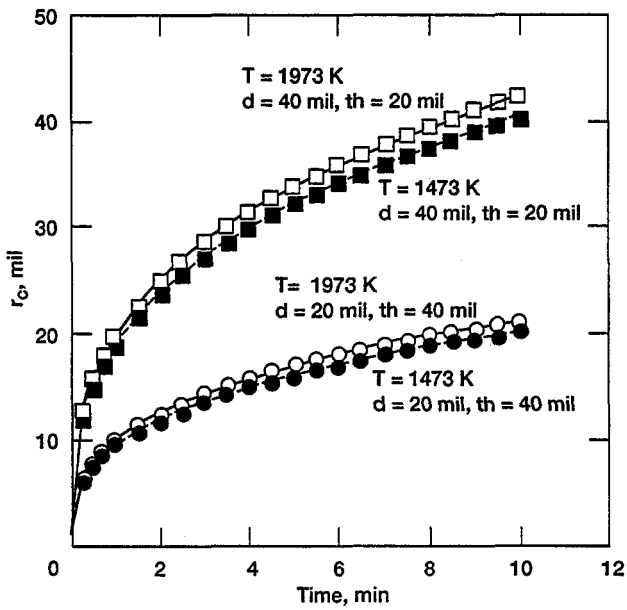

Figure B10.—Kinetics of formation of a cavity at the bottom of a pinhole at 1473 K and 1973 K.

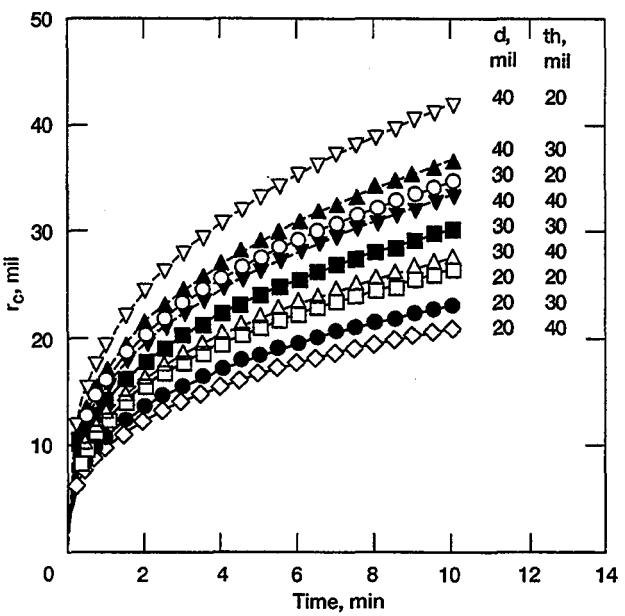

Figure B11.—Kinetics of formation of a cavity at the bottom of a pinhole at 1873 K.

REPORT DOCUMENTATION PAGE

Form Approved
OMB No. 0704-0188

1. AGENCY USE ONLY (*Leave blank*)	2. REPORT DATE	3. REPORT TYPE AND DATES COVERED
	January 1995	Technical Memorandum

4. TITLE AND SUBTITLE

Thermochemical Degradation Mechanisms for the Reinforced Carbon/Carbon Panels on the Space Shuttle

5. FUNDING NUMBERS

WU–505–63–52

6. AUTHOR(S)

Nathan S. Jacobson and Robert A. Rapp

7. PERFORMING ORGANIZATION NAME(S) AND ADDRESS(ES)

National Aeronautics and Space Administration
Lewis Research Center
Cleveland, Ohio 44135–3191

8. PERFORMING ORGANIZATION REPORT NUMBER

E–9256

9. SPONSORING/MONITORING AGENCY NAME(S) AND ADDRESS(ES)

National Aeronautics and Space Administration
Washington, D.C. 20546–0001

10. SPONSORING/MONITORING AGENCY REPORT NUMBER

NASA TM–106793

11. SUPPLEMENTARY NOTES

Nathan S. Jacobson, NASA Lewis Research Center and Robert A. Rapp, Department of Materials Science and Engineering, The Ohio State University, Columbus, Ohio 43210. Responsible person, Nathan S. Jacobson, organization code 5160, (216) 433–5498.

12a. DISTRIBUTION/AVAILABILITY STATEMENT

Unclassified - Unlimited
Subject Category 27

12b. DISTRIBUTION CODE

13. ABSTRACT ***(Maximum 200 words)***

The wing leading edge and nose cone of the Space Shuttle are fabricated from a reinforced carbon/carbon material (RCC). The material attains its oxidation resistance from a diffusion coating of SiC and a glass sealant. During re-entry, the RCC material is subjected to an oxidizing high temperature environment, which leads to degradation via several mechanisms. These mechanisms include oxidation to form a silica scale, reaction of the SiO_2 with the SiC to evolve gaseous products, viscous flow of the glass, and vaporization of the glass. Each of these is discussed in detail. Following extended service and many missions, the leading-edge wing surfaces have exhibited small pinholes. A chloridation/oxidation mechanism is proposed to arise from the NaCl deposited on the wings from the sea-salt laden air in Florida. This involves a local chloridation reaction of the SiC and subsequent re-oxidation at the external surface. Thermodynamic calculations indicate the feasibility of these reactions at active pits. Kinetic calculations predict pore depths close to those observed.

14. SUBJECT TERMS	15. NUMBER OF PAGES
Carbon/Carbon; Thermal protection; Silicon carbide; Oxidation; Corrosion	38
	16. PRICE CODE: A03

17. SECURITY CLASSIFICATION OF REPORT	18. SECURITY CLASSIFICATION OF THIS PAGE	19. SECURITY CLASSIFICATION OF ABSTRACT	20. LIMITATION OF ABSTRACT
Unclassified	Unclassified	Unclassified	

National Aeronautics and
Space Administration

Lewis Research Center
21000 Brookpark Rd.
Cleveland, OH 44135-3191